*remote sensing*

MDPI

*Article*

# A GRNN-Based Model for ERA5 PWV Adjustment with GNSS Observations Considering Seasonal and Geographic Variations

**Haoyun Pang [1,†], Lulu Zhang [2,†], Wen Liu [1], Xin Wang [3], Yuefeng Wang [1,*] and Liangke Huang [1]**

[1] College of Geomatics and Geoinformation, Guilin University of Technology, Guilin 541006, China; panghaoyun@glut.edu.cn (H.P.); 1020211832@glut.edu.cn (W.L.); lkhuang@whu.edu.cn (L.H.)
[2] College of Tourism and Landscape Architecture, Guilin University of Technology, Guilin 541006, China; 2020135@glut.edu.cn
[3] School of Space Science and Physics, Shandong University, Weihai 264209, China; 202321263@mail.sdu.edu.cn
* Correspondence: wangyuefeng2021@glut.edu.cn
† These authors contributed equally to this work.

**Abstract:** Precipitation water vapor (PWV) is an important parameter in numerical weather forecasting and climate research. However, existing PWV adjustment models lack comprehensive consideration of seasonal and geographic factors. This study utilized the General Regression Neural Network (GRNN) algorithm and Global Navigation Satellite System (GNSS) PWV in China to construct and evaluate European Centre for Medium-Range Weather Forecasts (ECMWF) Atmospheric Reanalysis (ERA5) PWV adjustment models for various seasons and subregions based on meteorological parameters (GMPW model) and non-meteorological parameters (GFPW model). A linear model (GLPW model) was established for model accuracy comparison. The results show that: (1) taking GNSS PWV as a reference, the Bias and root mean square error (RMSE) of the GLPW, GFPW, and GMPW models are about 0/1 mm, which better weakens the systematic error of ERA5 PWV. The overall Bias of the GLPW, GFPW, and GMPW models in the Northwest (NWC), North China (NC), Tibetan Plateau (TP), and South China (SC) subregions is approximately 0 mm after adjustment. The adjusted overall RMSE of the GLPW, GFPW, and GMPW models of the four subregions are 0.81/0.71/0.62 mm, 1.15/0.95/0.77 mm, 1.66/1.26/1.05 mm, and 2.11/1.35/0.96 mm, respectively. (2) The accuracy of the three models is tested using GNSS PWV, which is not involved in the modeling. The adjusted overall RMSE of the GLPW, GFPW, and GMPW models in the four subregions are 0.89/0.85/0.83 mm, 1.61/1.58/1.27 mm, 2.11/1.75/1.68 mm and 3.65/2.48/1.79 mm, respectively. As a result, the GFPW and GMPW models have better accuracy in adjusting ERA5 PWV than the linear model GLPW. Therefore, the GFPW and GMPW models can effectively contribute to water vapor monitoring and the integration of multiple PWV datasets.

**Keywords:** PWV; ERA5; GNSS; General Regression Neural Network



**Citation:** Pang, H.; Zhang, L.; Liu, W.; Wang, X.; Wang, Y.; Huang, L. A GRNN-Based Model for ERA5 PWV Adjustment with GNSS Observations Considering Seasonal and Geographic Variations. *Remote Sens.* **2024**, *16*, 2424. https://doi.org/10.3390/rs16132424

Academic Editors: Robert Odolinski and Baocheng Zhang

Received: 17 May 2024
Revised: 22 June 2024
Accepted: 25 June 2024
Published: 1 July 2024



## 1. Introduction

Atmospheric water vapor plays an important role in global atmospheric radiation, water cycle, and energy balance. High-precision water vapor data are helpful in monitoring and forecasting severe weather such as rainstorms, cold currents, typhoons, major droughts, and waterlogging disasters [1–3]. Besides being an indicator of climate change, water vapor in the atmosphere affects the refractivity of radio signals and thus becomes a major error source in radio-based geodetic techniques [4].

Precipitable water vapor (PWV) is commonly used to describe the content of water vapor in the atmosphere and can be retrieved from observations and models [5,6]. With the development of PWV detection technology, the data sources of PWV products are becoming more abundant, such as radiosonde (RS), Global Navigation Satellite System (GNSS), satellite sensors, and atmospheric reanalysis data [7–12]. While RS sites can provide high-precision PWV data and are commonly used to assess the accuracy of other PWV

products, they are limited in their ability to depict the spatiotemporal variation of water vapor due to their high cost, sparse distribution and low temporal resolution [13,14]. The GNSS water vapor inversion method proposed by Bevis [15] is widely applied due to its advantages, including all-weather observation, high spatiotemporal resolution, and low cost [16,17]. Despite being high-precision point data, both RS and GNSS data require spatial interpolation for their extended application in climate research [18]. Remote sensing water vapor inversion can depict the regional distribution of atmospheric water vapor, but it possesses limited temporal resolution and necessitates clear and cloudless atmospheric observation conditions [19]. The PWV products of atmospheric reanalysis data have a long time scale and comprehensive spatial coverage, but the accuracy and reliability of the areas with few or missing assimilation data need further improvement [20].

The single detection method cannot provide high-precision water vapor information due to systematic Bias stemming from differences in temporal and spatial resolutions and coverage. Therefore, multisource data fusion is introduced to overcome the above limitations of detection technology, including system Bias adjustment and the optimization of unbiased datasets [21,22]. Khaniani et al. [23] found that the deviation between Moderate-Resolution Imaging Spectroradiometer (MODIS) PWV and 38 GNSS-derived PWV in Iran is linear with the site's height and established a highly correlated linear model, which reduces the error of MODIS PWV. Bai et al. [24] evaluated the MODIS PWV and the fifth-generation European Centre for Medium-Range Weather Forecasts (ECMWF) Atmospheric Reanalysis (ERA5) PWV of 260 Chinese GNSS sites and established a MODIS PWV linear adjustment model considering climate and regional differences. Zhu et al. [25] evaluated the MODIS PWV against GNSS PWV and the ERA5 PWV from 2013 to 2018 in China and established a Chinese regional PWV adjustment model according to the annual and semi-annual characteristics of MODIS PWV and ERA5 PWV deviations at each grid point. Wang, XZ et al. [26] proposed a new empirical PWV grid model called ASV-PWV, which uses the zenith wet delay from the Askne model and is improved by spherical harmonics and vertical adjustment. Alshawaf et al. [27] used the fixed-rank Kriging interpolation method to fuse PWV datasets, including GNSS, Interferometric Synthetic Aperture Radar (In SAR), and Weather Research and Forecasting (WRF) modeling system. Shikhovtsev et al. [28] proposed a PWV correction method that takes the underlying surface into account, using the Precipitation water vapor content decays exponentially with altitude and based on the average altitude of the grid nodes around the location.

Moreover, scholars have studied the PWV adjustment model based on machine learning algorithms due to the inevitable deviation caused by the imperfection of the assumptions behind the interpolation methods [29,30]. The quality of MODIS PWV data in China is poor and not suitable for studying subtle variations in PWV. WANG LiLi et al. [31] pointed out that the comprehensive utilization rate and applicability of MODIS products vary significantly across different subregions, with particularly low utilization rates of MODIS data in the Qinghai-Tibet Plateau. Lu et al. [32] constructed the convolutional neural network (CNN) fusion model of MODIS PWV and ERA5 PWV on the west coast of America and claimed that the fused PWV was in good agreement with the GNSS PWV. Taking GNSS as the reference value, Xiong et al. [33] employed three methods—Random Forest (RF), Generalized Regression Neural Network (GRNN), and Back Propagation Neural Network (BPNN)—to construct MODIS PWV adjustment models for the Chinese region separately on both monthly and annual scales. Ma et al. [34] combined the water vapor data from the FengYun-3 meteorological satellite's Moderate-Resolution Spectral Imager (MERSI) with various geospatial data to establish a PWV GRNN model for the San-Jiang-yuan area of China and proposed a daily systematic error adjustment method for reconstructing MERSI PWV based on GNSS PWV.

Currently, the linear models of ERA5 [35] and MODIS [36] are adjusted with GNSS and have experienced a transformation from a single-factor linear model to a multi-factor linear model, but it also requires a large amount of factor data and has low accuracy [37]. With the development of artificial intelligence, machine learning has shown strong nonlinear

model-building advantages with superior performance [38,39]. This study constructs the adjustment models of meteorological and non-meteorological parameters based on the General Regression Neural Network (GRNN) method for the entire China region and four subregions by utilizing PWV values derived from GNSS and ERA5. Moreover, we analyze the correlation between multiple meteorological parameters and PWV values to establish a suitable meteorological adjustment model, considering the complex seasonality and geographic variations of water vapor in China. To test the performance of the model, the 10-fold cross-validation (CV) technique [40] is employed. Bias, standard deviation (STD), root mean square error (RMSE), and correlation coefficient (R) are used as criteria to assess the performance [41]. The aim of this study is to provide a more important reference for the construction of regional moisture fusion products in China.

## 2. PWV Data and Processing

### *2.1. GNSS PWV*

The diverse topography and intricate climate of China's land area result in complex variations in PWV. To facilitate the discussion on spatiotemporal PWV variability and the accuracy of the water vapor adjustment model, the China region is divided into four subregions: North China (NC), South China (SC), Tibet Plateau (TP), and Northwest China (NWC). The study area and site distribution are shown in Figure 1.

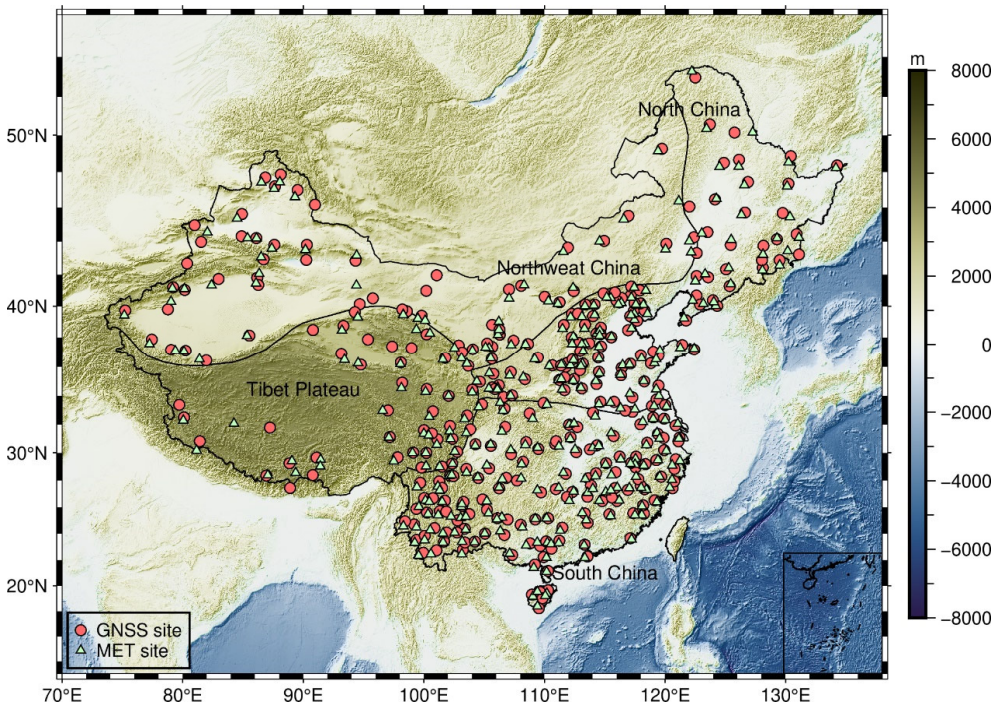


**Figure 1.** Distribution of 339 GNSS and MET sites and four subregions in China from 2016 to 2018.

Adhering to the criterion of the data time series greater than 60%, this study selected hourly observations of 339 GNSS sites from the Crustal Movement Observation Network of China (CMONC) from 2016 to 2018. We selected the MET sites closest to the GNSS site in the China Meteorological Administration (CMA) and used the hourly meteorological parameters of the site to conduct correlation analysis and use them as input factors to build the ERA5 PWV adjustment models.

The GNSS zenith total delay (ZTD) is the sum of the zenith hydrostatic delay (ZHD) and the zenith wet delay (ZWD). The ZHD could be obtained by the Saastamoinen model [24].

$$\mathrm{ZTD} = \mathrm{ZHD} + \mathrm{ZWD}, \quad (1)$$

$$\mathrm{ZHD} = \frac{0.0022767 \times \mathrm{P_s}}{1 - 0.00266\cos\varphi - 0.00028 \times \mathrm{h_o}}, \tag{2}$$

where $\mathrm{P_s}$, $\varphi$ and $\mathrm{h_o}$ are the surface pressure (hPa) of the MET site, the latitude (radians), and the elevation (km) of the GNSS site, respectively.

$$\mathrm{PWV} = \frac{10^6}{\rho_w \mathrm{R_v}\left[\frac{\mathrm{k_3}}{\mathrm{T_m}} + \mathrm{k_2'}\right]} \cdot \mathrm{ZWD}\,, \tag{3}$$

where $\rho_w$ is the density of liquid water ($1 \times 10^3$ kg/m$^3$), $\mathrm{R_v}$ is the water vapor gas constant (461.495 J·kg$^{-1}$·k$^{-1}$), $\mathrm{k_2'}$ and $\mathrm{k_3}$ are the empirical values ($\mathrm{k_2'} = 22.13 \pm 2.20$ K/hPa, $\mathrm{k_3} = (3.739 \pm 0.012) \times 10^5$ K$^2$/hPa). $\mathrm{T_m}$ is the atmospheric weighted mean calculated by the Chinese empirical regionalization model, and the additional information about the procedure can be found in Huang et al. [25].

$$\begin{aligned}\mathrm{T_m}(\mathrm{T_s}, \mathrm{h_0}, \varphi, \mathrm{DOY}) = {} & \mathrm{a_0} + \mathrm{a_1}\mathrm{T_s} + \mathrm{a_2 h} + \mathrm{a_3}\varphi + \mathrm{b_1}\cos\left(\tfrac{\mathrm{DOY}}{365.25}\cdot 2\pi\right) \\ & + \mathrm{b_2}\sin\left(\tfrac{\mathrm{DOY}}{365.25}\cdot 2\pi\right) + \mathrm{b_3}\cos\left(\tfrac{\mathrm{DOY}}{365.25}\cdot 4\pi\right) + \mathrm{b_4}\sin\left(\tfrac{\mathrm{DOY}}{365.25}\cdot 4\pi\right)\end{aligned}, \tag{4}$$

where $\mathrm{T_s}$ is the surface temperature of the MET site, DOY is day of the year. $\mathrm{a_0}$, $\mathrm{a_1}$, $\mathrm{a_2}$, $\mathrm{a_3}$, $\mathrm{b_1}$, $\mathrm{b_2}$, $\mathrm{b_3}$ and $\mathrm{b_4}$ are the model coefficients.

### *2.2. ERA5 PWV*

ERA5 reanalysis data are ECMWF's fifth-generation global climate reanalysis data set and its latest generation of atmospheric reanalysis products [42]. ERA5 is generated using the 4D-Var data assimilation scheme in the CY41R2 model of ECMWF's comprehensive forecasting system, with high spatial and temporal resolution. Its time resolution is 1 h, and its horizontal spatial resolution is 0.25° × 0.25° (longitude × latitude, about 31 km) [43–45]. Using GNSS data as the reference value for evaluating ERA5 PWV, the results show that the correlation coefficient, Bias, and RMSE in China are 0.99 mm, 0.38 mm, and 1.99 mm, respectively [46]. When applied to South China, the average performance makes a big difference. In addition, we vertically correct and horizontally interpolate the PWV of the four closest ERA5 grid points around the GNSS site [47].

### *2.3. RS PWV*

The RS dataset, collected by radiosondes daily at 00:00 and 12:00 UTC, includes vertical atmospheric data. Each radiosonde site mentions stratified meteorological parameters such as air pressure, temperature, and relative humidity from the ground to about 30 km above the Earth's surface [48,49]. In addition, the meteorological data of each pressure layer directly provided by the radiosonde are used to obtain the PWV data of the site surface through integration and summation. In this study, we used the PWV of the RS stratification in 2018 as the reference value to evaluate the accuracy of the vertical adjustment models. RS profiles can be accessed from the upper air archives on the University of Wyoming (UW) website [50–52].

$$\mathrm{PWV} = \frac{1}{\mathrm{g}}\int_{\mathrm{P_i}}^{\mathrm{P_{i+1}}} \frac{0.622\mathrm{e}}{\mathrm{P} - \mathrm{e}}\mathrm{dP}, \tag{5}$$

$$\mathrm{e} = 6.112 \cdot \exp\left(\frac{17.6\mathrm{T_d}}{\mathrm{T_d} + 243.15}\right), \tag{6}$$

where $\mathrm{P_i}$ and $\mathrm{P_{i+1}}$ are the pressure (Pa) at the lower and upper layers, respectively. g is the acceleration of gravity, e is the vapor pressure (Pa), and $\mathrm{T_d}$ is dew point temperature (°C).

$$\mathrm{PWV_t} = \mathrm{PWV_r} \times \exp(\mathrm{r}(\mathrm{h_t} - \mathrm{h_r})), \tag{7}$$

$$r = \beta_0 + \beta_1 \cos\left(\frac{DOY}{365.25}\cdot 2\pi\right) + \beta_2 \sin\left(\frac{DOY}{365.25}\cdot 2\pi\right) + \beta_3 \cos\left(\frac{DOY}{365.25}\cdot 4\pi\right) + \beta_4 \sin\left(\frac{DOY}{365.25}\cdot 4\pi\right), \quad (8)$$

where $PWV_t$ and $PWV_r$ are the PWV value (mm) at different heights (km) $h_t$ and $h_r$, respectively. r is PWV lapse rate (mm/km), which is the key factor for vertical water vapor adjustment. $\beta_0$, $\beta_1$, $\beta_2$, $\beta_3$ and $\beta_4$ are the model coefficients.

The distribution of water vapor is significantly different in the vertical direction, following an exponential decay trend with increasing height [53]. The PWV vertical adjustment model is crucial to the study of water vapor. Therefore, it is necessary to select the PWV vertical adjustment model to ensure data accuracy before constructing the water vapor adjustment model [54]. We established water vapor adjustment models for the entire subregion and subregions (CT-PWV) based on the PWV profiles of 88 RS sites from 2012 to 2017. Furthermore, RS PWV profiles for 2018 were used as the true values, while the model CT-PWV, the traditional adjustment model (E-PWV) with a constant lapse rate of −0.5 mm/km [46], and the adjustment model C-PWV [55] built on the ERA5 dataset were used as reference values. The coefficients of the CT-PWV model, fitted using the least squares method, and the accuracy statistics are shown in Tables 1 and 2, respectively.

**Table 1.** Coefficients of vertical adjustment model CT-PWV.

| Model | Subregion | $\beta_0$ | $\beta_1$ | $\beta_2$ | $\beta_3$ | $\beta_4$ |
|---|---|---|---|---|---|---|
| CT-PWV | China | −0.4278 | −0.0198 | −0.0024 | 0.0054 | 0.0016 |
| | NWC | −0.3875 | −0.0080 | 0.0041 | −0.0004 | −0.0046 |
| | TP | −0.5143 | −0.0194 | −0.0060 | 0.0169 | 0.0053 |
| | NC | −0.4222 | 0.0159 | 0.0122 | 0.0153 | 0.0079 |
| | SC | −0.4346 | −0.0438 | −0.0123 | 0.0015 | 0.0014 |

**Table 2.** Vertical interpolation accuracy statistics of models E-PWV, C-PWV, and CT-PWV using 2018 RS PWV profile data.

| Subregion | Model | Bias (mm) | | | RMSE (mm) | | |
|---|---|---|---|---|---|---|---|
| | | Mean | Min | Max | Mean | Min | Max |
| NWC | E-PWV | −1.91 | −3.39 | −0.68 | 3.39 | 1.2 | 6.23 |
| | C-PWV | −0.03 | −0.26 | 0.28 | 1.09 | 0.52 | 1.81 |
| | CT-PWV | 0.30 | −0.09 | 0.77 | 1.24 | 0.52 | 2.21 |
| TP | E-PWV | −3.06 | −4.46 | −0.58 | 4.87 | 1.06 | 6.54 |
| | C-PWV | −0.63 | −1.20 | 0.07 | 1.53 | 0.50 | 2.09 |
| | CT-PWV | −0.21 | −0.66 | 0.48 | 1.17 | 0.37 | 2.29 |
| NC | E-PWV | −2.49 | −5.12 | −0.96 | 4.50 | 1.98 | 8.25 |
| | C-PWV | −0.24 | −0.58 | −0.07 | 1.44 | 0.90 | 2.99 |
| | CT-PWV | 0.21 | −0.13 | 0.84 | 1.53 | 0.79 | 3.68 |
| SC | E-PWV | −4.67 | −8.70 | −1.43 | 7.09 | 2.73 | 11.89 |
| | C-PWV | −0.32 | −0.86 | 0.24 | 2.00 | 1.19 | 3.17 |
| | CT-PWV | 0.47 | −0.21 | 1.68 | 2.26 | 1.12 | 3.71 |
| China | E-PWV | −3.32 | −8.70 | −3.32 | 5.40 | 1.57 | 11.89 |
| | C-PWV | −0.26 | −1.11 | −0.27 | 1.59 | 0.68 | 2.99 |
| | CT-PWV | 0.30 | −0.56 | 1.68 | 1.74 | 0.43 | 3.71 |

As shown in Table 2, the mean Bias and mean RMSE of the E-PWV, C-PWV, and CT-PWV models in China are −3.32/5.4 mm, −0.26/1.59 mm and 0.30/1.74 mm, respectively. For Bias, the C-PWV model shows a small Bias fluctuation range, and its adjustment accuracy in China and four subregions is more stable compared to the E-PWV and CT-PWV models. For RMSE, the C-PWV model shows better adjustment accuracy in the NWC, NC, and SC subregions compared with the other two models, while the CT-PWV model shows the best adjustment accuracy in the TP subregion. In the SC and NC subregions, the range

of the maximum value of RMSE after vertical adjustment by the C-PWV and CT-PWV models is 3–4 mm, while the maximum RMSE by the E-PWV model is 11.89 mm. Therefore, this study selected the C-PWV model to perform spatial adjustment of PWV.

## 3. Methodology

### *3.1. Generalized Regression Neural Network*

The General Regression Neural Network (GRNN) method shows good accuracy in building water vapor adjustment models [33,56]. GRNN is a regression neural network designed for nonlinear mapping and pattern recognition tasks proposed by Donald F. Specht in 1991 [57]. The algorithm comprehends intricate nonlinear relationships inherent in complex datasets and excels in capturing the underlying patterns that may elude traditional linear models. GRNN employs a radial basis function to model the input-output relationships, with a unique smoothing parameter that controls the spread of the radial basis functions [58]. Moreover, GRNN demonstrates rapid overall convergence characteristics as it operates as a feedforward neural network, eliminating the need for the iterative process employed in backpropagation networks. These advantages have made GRNN a powerful tool for regression, approximation, fitting, and prediction.

GRNN consists of four layers: input layer, pattern layer, summation layer, and output layer. The input layer consists of p neuron outputs, which are consistent with the dimensions of the input support x and are continuous with the pattern layer. The pattern layer has n nodes, the number of nodes is equal to the number of training samples, and the value of the Gaussian function of each sample is calculated. The output of the pattern single layer is sent to the summation layer. The summation layer calculates the sum of $Y^I K\left(X, X^i\right)$ and the sum of $K\left(X, X^i\right)$, both of which are sent to the output layer. The number of neurons in the output layer is equal to the dimension supported by the output in the learning sample. The output layer receives the output of the summation layer and estimates $\hat{Y}(X)$:

$$E(y|x) = \frac{\int_{-\infty}^{\infty} yf(x,y)dy}{\int_{-\infty}^{\infty} f(x,y)dy}, \tag{9}$$

In reality, the PDF $f(x, y)$ is unknown and can be obtained through non-parametric estimation based on observed samples of x and y. $\hat{f}(X, Y)$ can be estimated by:

$$\hat{f}(X,Y) = \frac{1}{(2\pi)^{(p+1)/2}\sigma^{(p+1)}}\frac{1}{n} \times \sum_{i=1}^{n} \exp\left[-\frac{\left(X-X^i\right)^T\left(X-X^i\right)}{2\sigma^2}\right] \exp\left[-\frac{\left(Y-Y^i\right)^2}{2\sigma^2}\right], \tag{10}$$

where n is the number of sample observations, p is the dimensionality of the random variable x, $\sigma$ is spread parameter which is the only unknown parameter in GRNN. $X^i$ and $Y^i$ represent the observed values of the random variables X and Y, respectively. Then, define a scalar function $D_i^2$ and a Gaussian kernel:

$$D_i^2 = \left(X-X^i\right)^T\left(X-X^i\right), \tag{11}$$

$$K\left(X, X^i\right) = \exp\left(-\frac{D_i^2}{2\sigma^2}\right), \tag{12}$$

By combining Equations (9)–(12), we will obtain:

$$\hat{Y}(X) = \frac{\sum_{i=1}^{n} Y^i K\left(X, X^i\right)}{\sum_{i=1}^{n} K\left(X, X^i\right)}, \tag{13}$$

The GRNN algorithm consists of four layers: an input layer, a pattern layer, a summation layer, and an output layer.

### *3.2. Correlation Analysis and Parameter Selection*

The variations in PWV are influenced by geographical factors, such as latitude, sea and land distribution, and altitude, exhibiting distinct temporal characteristics, including seasonality and periodic changes [59]. Therefore, we first used longitude, latitude, altitude, Day of Year (DOY), and Hour of Day (HOD) as basic model-influencing factors.

In the context of the atmospheric moisture cycle, the transportation of water vapor resulting from rainfall, evaporation, and atmospheric circulation contributes to fluctuations in PWV. The atmospheric precipitation and evaporation processes are influenced by four fundamental meteorological elements: pressure, temperature, humidity, and wind. In this study, we employed the Spearman [60,61] correlation coefficient as a metric to investigate the correlations among 2016–2018 China's hourly GNSS PWV, ERA5 PWV, and four highly associated meteorological elements at meteorological sites: temperature (T), pressure (P), relative humidity (RH) and precipitation (PRE). The correlation values of the above six factors are shown in Figure 2.

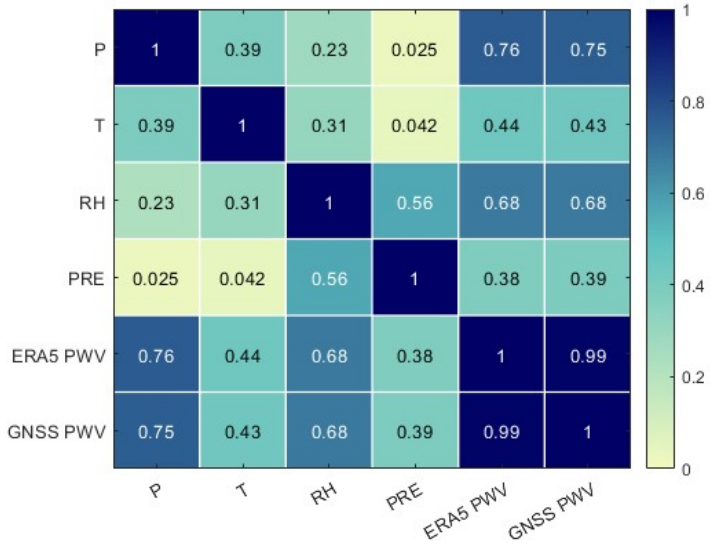


**Figure 2.** Cross-correlations among the GNSS PWV, ERA5 PWV, and multisource meteorological parameters of meteorological sites from 2016 to 2018 in China.

Correlation between parameters is evaluated using the standard R-absolute value, falling into 0.7–1 for strong correlation, 0.4–0.7 for moderate correlation, and 0–0.4 defined as weak correlation. In Figure 2, the correlation coefficient between GNSS PWV and ERA5 PWV is 0.99, indicating that the two datasets are highly correlated and ensure data quality for training GRNN models. The correlation coefficients between the ERA5 PWV, GNSS PWV data sets, and air pressure are 0.76/0.75, the correlation coefficients with temperature are 0.44/0.43, and the correlation coefficients with precipitation are 0.38/0.39. The correlation coefficient between the PWV data set and the two humidities is 0.68. Higher values of relative humidity are robustly associated with increased atmospheric water vapor content, explaining the correlation between the meteorological parameters and PWV. The complex atmospheric thermodynamic circulation mechanism and heavy rainfall affect the dramatic changes in atmospheric water vapor, which may be the main reason for the weak correlation between the PWV and precipitation [62,63]. Therefore, we introduced three meteorological elements: pressure, temperature, and relative humidity, to participate in constructing the PWV adjustment model.

### 3.3. Model Construction

Utilizing the GRNN algorithm [64], we selected 80% of the 339 GNSS sites to construct the ERA5 PWV adjustment models: the linear model (GLPW), the foundational PWV adjustment model excluding meteorological factors (GFPW model), and the PWV adjustment model integrating multisource parameters (GMPW model) [65,66]. We used the remaining 20% of GNSS site data to test the accuracy of these ERA5 PWV adjustment models. The architecture of GFPW and GMPW models are shown in Figure 3. The input layer of the GFPW model consists of six neurons: latitude, longitude, altitude, DOY, HOD, and ERA5 PWV. The input layer of the GMPW model includes nine neurons representing latitude, longitude, altitude, DOY, HOD, ERA5 PWV, P, T, and RH. The output layer of the two models consists of one neuron: GNSS PWV.

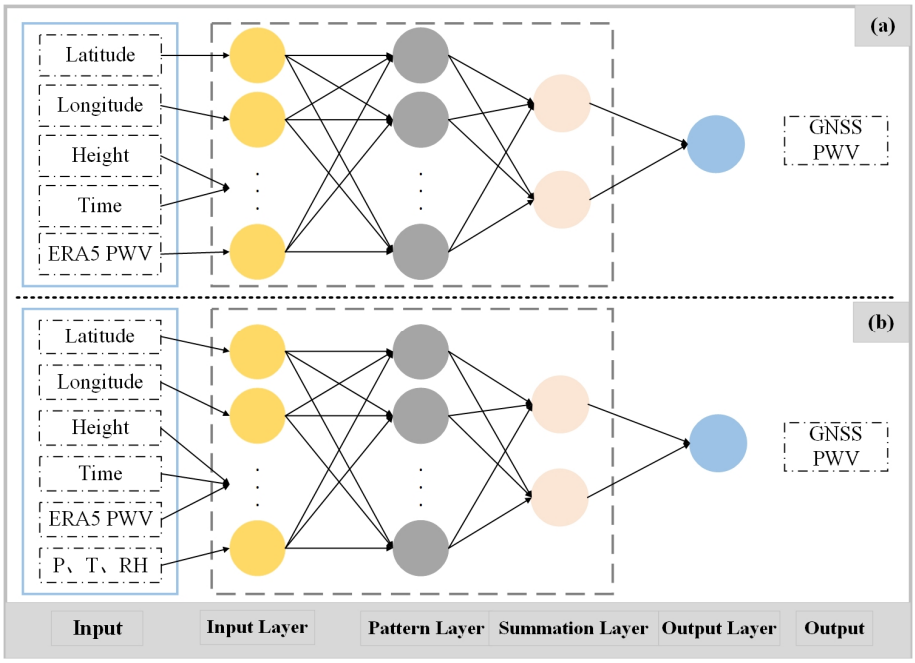


**Figure 3.** Architecture of the models GFPW (**a**) and GMPW (**b**) adjusting ERA5 PWV by GNSS PWV.

Before constructing the PWV adjustment model using the GRNN algorithm, it is essential to perform registration and quality control between different datasets. We employed a threshold based on three times the standard deviation of the Bias between GNSS PWV and ERA5 PWV to eliminate associated outliers and obtain the GNSS-ERA5 data pair. In addition, the input vectors used for model construction are normalized [−1,1] to eliminate the influence of different units and values on modeling results. Moreover, constructing the PWV adjustment model based on GRNN requires determining the optimal spread parameter $\sigma$ that significantly influences the model's performance. Building upon previous studies, we specified the range of $\sigma$ from 0.01 to 0.1 with steps of 0.01 and determined the optimal value of $\sigma$ using the smallest RMS generated from a 10-fold cross-validation [67,68]. The variation of optimal values of $\sigma$ and RMSE during 10-fold cross-validation for the GFPW model in the spring NWC subregion is shown in Figure 4.

As shown in Figure 4, the RMSE initially decreases and then increases with the augmentation of $\sigma$, reaching its minimum at $\sigma = 0.02$. Consequently, $\sigma = 0.02$ is chosen to construct the optimal PWV adjustment model based on GRNN. Given the regional disparities and seasonal fluctuations in PWV, models GFPW and GMPW were constructed and compared, accounting for diverse geographical subregions and varying seasons. The four seasons are defined as follows: spring is from March to May, summer is from June to August, fall is from September to November, and winter is from December to February. The

optimal spread parameters $\sigma$ and their corresponding accuracies for models GFPW and GMPW in four subregions and four seasons are presented in Tables 3 and 4, respectively.

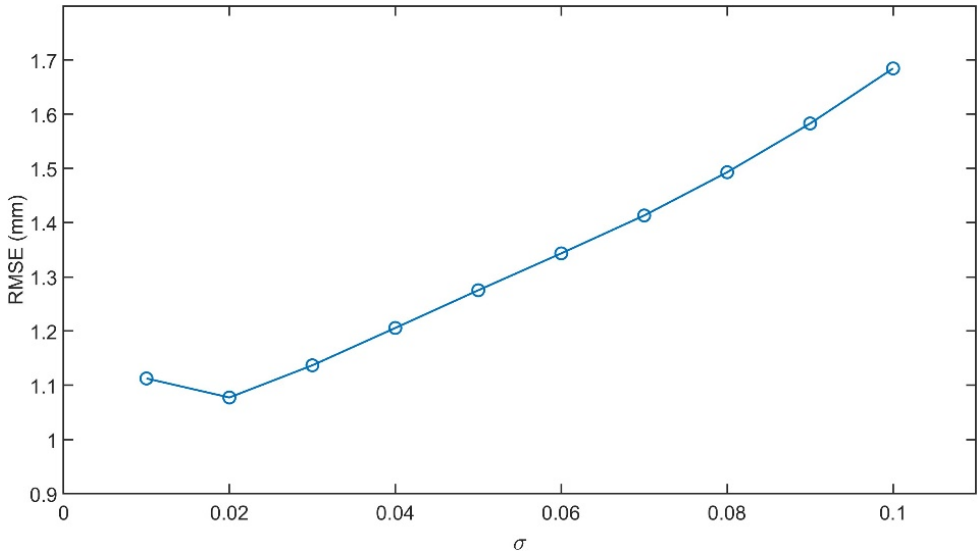


**Figure 4.** GFPW Model for the NWC Subregion in Spring: changes in RMSE values $\sigma$ under different distribution parameters generated by 10-fold cross-validation.

**Table 3.** The optimal spread parameters $\sigma$ of models GMPW and GFPW in various subregions and four seasons.

| Subregion | Spring | | Summer | | Fall | | Winter | |
|---|---|---|---|---|---|---|---|---|
| | GMPW | GFPW | GMPW | GFPW | GMPW | GFPW | GMPW | GFPW |
| NWC | 0.04 | 0.02 | 0.01 | 0.01 | 0.03 | 0.01 | 0.06 | 0.01 |
| TP | 0.07 | 0.01 | 0.01 | 0.01 | 0.03 | 0.01 | 0.01 | 0.01 |
| NC | 0.08 | 0.02 | 0.01 | 0.02 | 0.02 | 0.01 | 0.02 | 0.01 |
| SC | 0.02 | 0.02 | 0.01 | 0.01 | 0.03 | 0.01 | 0.01 | 0.01 |
| China | 0.04 | 0.01 | 0.04 | 0.01 | 0.03 | 0.01 | 0.03 | 0.01 |

**Table 4.** The cross-validation (CV) accuracy of models GMPW and GFPW in various subregions and four seasons (The unit is mm, and the asterisk (*) represents '$\times 10^{-3}$').

| Subregion | | Spring CV | | Summer CV | | Fall CV | | Winter CV | |
|---|---|---|---|---|---|---|---|---|---|
| | | GMPW | GFPW | GMPW | GFPW | GMPW | GFPW | GMPW | GFPW |
| NWC | Bias | 8 * | 5 * | 0.03 | −3 * | 0.5 * | −0.3 * | −4 * | 1 * |
| | MAE | 0.68 | 0.75 | 1.31 | 1.11 | 0.75 | 0.75 | 0.45 | 0.44 |
| | RMSE | 0.96 | 1.04 | 1.81 | 1.51 | 1.03 | 1.05 | 0.58 | 0.6 |
| TP | Bias | 0.01 | 2.9 * | 0.04 | 8 * | 0.02 | −0.4 * | 0.01 | −1 * |
| | MAE | 0.87 | 0.85 | 1.29 | 1.13 | 0.85 | 0.97 | 0.67 | 0.67 |
| | RMSE | 1.15 | 1.24 | 1.76 | 1.68 | 1.19 | 1.44 | 0.94 | 1.02 |
| NC | Bias | −0.01 | −2 * | 0.07 | −0.01 | 0.01 | −2 * | 0.01 | 1 * |
| | MAE | 1.37 | 1.12 | 1.87 | 1.59 | 1.16 | 1.07 | 0.71 | 0.67 |
| | RMSE | 1.77 | 1.61 | 2.37 | 2.11 | 1.61 | 1.53 | 0.97 | 1.05 |
| SC | Bias | 0.04 | 2 * | 0.03 | 3 * | 0.03 | 6 * | 0.02 | −2 * |
| | MAE | 1.38 | 1.29 | 1.65 | 1.44 | 1.18 | 1.13 | 1.01 | 0.94 |
| | RMSE | 1.91 | 1.74 | 2.3 | 1.97 | 1.65 | 1.59 | 1.42 | 1.35 |
| CH | Bias | 1 * | 2 * | 0.04 | −0.1 * | 0.01 | 0.8 * | 9 * | −0.5 * |
| | MAE | 1.07 | 1.00 | 1.53 | 1.31 | 0.98 | 0.98 | 0.71 | 0.68 |
| | RMSE | 1.44 | 1.40 | 2.06 | 1.81 | 1.37 | 1.40 | 0.97 | 1.00 |

To better compare the results with those of other similar studies [69], we also established a classic ERA5 PWV linear adjustment model (GLPW), the model formula, and the model factors a and b in Table 5:

$$\text{GNSS PWV} = \text{a} \times \text{ERA5 PWV} + \text{b}, \quad (14)$$

where a and b are the model coefficients.

**Table 5.** The model coefficients (a and b) of models GLPW in various subregions and four seasons.

| Subregion | | Spring | Summer | Fall | Winter |
|---|---|---|---|---|---|
| NWC | a | 0.96 | 0.96 | 0.97 | 0.86 |
| | b | 0.32 | 1.16 | 0.35 | 0.53 |
| TP | a | 0.98 | 0.99 | 1.01 | 0.96 |
| | b | 0.85 | 1.44 | 0.53 | 0.29 |
| NC | a | 1.02 | 1.01 | 1.02 | 1.00 |
| | b | −0.25 | 0.59 | −0.20 | −0.13 |
| SC | a | 1.00 | 0.98 | 1.01 | 1.00 |
| | b | 0.58 | 2.22 | 0.32 | −0.16 |
| China | a | 1.01 | 1.00 | 1.02 | 0.99 |
| | b | 0.14 | 0.84 | 0.08 | 0.003 |

## 4. Precision Assessment and Analysis

### *4.1. Overall Accuracy*

Take GNSS PWV as the reference, the Bias, MAE, and RMSE [70] between ERA5 PWV adjusted by models GLPW, GFPW, and GMPW and the unadjusted ERA5 PWV are compiled in Table 6. The variations of these metrics across different subregions and four seasons are depicted in Figures 5 and 6.

**Table 6.** The accuracy statistics between the unadjusted ERA5 PWV and ERA5 PWV adjusted by GLPW, GFPW, and GMPW models using GNSS PWV as the reference (The unit is mm, the asterisk (*) represents '$\times 10^{-3}$', and the UA represents 'Unadjusted').

| Subregion | | Bias | | | | MAE | | | | RMSE | | | |
|---|---|---|---|---|---|---|---|---|---|---|---|---|---|
| | | UA | GLPW | GFPW | GMPW | UA | GLPW | GFPW | GMPW | UA | GLPW | GFPW | GMPW |
| NWC | Spring | 0.06 | 0.04 | 4 * | 1 * | 1.15 | 1.13 | 0.62 | 0.29 | 1.43 | 0.83 | 0.71 | 0.57 |
| | Summer | −0.35 | −0.20 | 0.03 | 0.03 * | 1.75 | 1.71 | 0.72 | 0.02 | 2.09 | 1.07 | 0.98 | 0.83 |
| | Fall | −0.06 | −0.06 | 4 * | 0.01 | 1.13 | 1.1 | 0.62 | 0.49 | 1.4 | 0.84 | 0.65 | 0.64 |
| | Winter | −0.06 | 0.05 | 0.02 | 0.01 | 0.76 | 0.68 | 0.41 | 0.37 | 0.92 | 0.53 | 0.48 | 0.46 |
| TP | Spring | −0.63 | 0.35 | 3 * | 0.03 | 1.63 | 1.39 | 0.72 | 0.64 | 1.73 | 1.04 | 0.93 | 0.86 |
| | Summer | −1.24 | 0.35 | 0.01 | 0.05 * | 2.23 | 2.02 | 0.84 | 0.04 | 2.42 | 1.34 | 0.92 | 0.84 |
| | Fall | −0.62 | 0.42 | 9 * | 4 * | 1.75 | 1.47 | 0.86 | 0.33 | 1.82 | 1.16 | 1.15 | 0.88 |
| | Winter | −0.10 | 0.49 | 4 * | 0.06 * | 1.29 | 1.07 | 0.6 | 0.03 | 1.33 | 1.08 | 0.8 | 0.51 |
| NC | Spring | −0.08 | −0.08 | 0.03 | −0.01 | 1.42 | 1.27 | 1.26 | 0.96 | 1.85 | 1.62 | 1.29 | 1.17 |
| | Summer | −0.86 | 0.29 | 0.5 | 0.41 | 2.2 | 2 | 1.7 | 1.33 | 2.73 | 2.15 | 1.88 | 1.74 |
| | Fall | −0.24 | 0.17 | −0.04 | 0.01 | 1.38 | 1.22 | 0.86 | 0.44 | 1.81 | 1.77 | 1.36 | 0.82 |
| | Winter | 0.12 | 0.08 | 4 * | 1 * | 0.87 | 0.74 | 0.55 | 0.18 | 1.17 | 1.13 | 0.53 | 0.48 |
| SC | Spring | −0.57 | −0.06 | 0.01 | 0.01 | 1.89 | 1.8 | 1.03 | 0.55 | 2.36 | 2.14 | 1.34 | 0.98 |
| | Summer | −1.42 | −0.15 | −0.4 * | 3 * | 2.43 | 2.28 | 1 | 0.41 | 2.86 | 2.7 | 1.42 | 1.03 |
| | Fall | −0.70 | −0.09 | 0.01 | 0.01 | 1.89 | 1.89 | 0.75 | 0.46 | 2.59 | 2.03 | 1.48 | 1.07 |
| | Winter | 0.31 | −0.21 | 0.01 | 2 * | 1.43 | 1.35 | 0.75 | 0.1 | 1.99 | 1.91 | 1.19 | 0.76 |
| China | Spring | −0.31 | 0.13 | 0.02 | 0.01 | 1.44 | 1.49 | 0.81 | 0.61 | 1.84 | 1.40 | 1.06 | 0.89 |
| | Summer | −0.97 | 0.16 | 0.11 | 0.02 | 2.09 | 2.08 | 0.97 | 0.45 | 2.52 | 1.81 | 1.3 | 1.11 |
| | Fall | −0.40 | 0.11 | 0.01 | 4 * | 1.46 | 1.47 | 0.77 | 0.43 | 1.90 | 1.45 | 1.16 | 0.855 |
| | Winter | 0.02 | 0.07 | 0.01 | 4 * | 1.01 | 1.01 | 0.57 | 0.17 | 1.35 | 1.16 | 0.75 | 0.55 |

As shown in Table 6, the Bias adjusted by the models GLPW, GFPW, and GMPW are basically close to 0 mm, which shows that the systematic differences between ERA5 PWV and GNSS PWV are basically eliminated. For MAE, the ranges of the GLPW model in the NWC, TP, NC, and SC subregions are 0.68–1.71 mm, 1.07–2.02 mm, 0.74–2.00 mm, and 1.35–2.28 mm, respectively. For MAE, the ranges of the GFPW model in the NWC, TP, NC, and SC subregions are 0.41–0.72 mm, 0.60–0.86 mm, 0.55–1.70 mm, and 0.75–1.03 mm, respectively, while the value range of the GMPW model is 0.02–0.49 mm, 0.03–0.64 mm, 0.18–1.33 mm and 0.10–0.55 mm. Compared with unadjusted ERA5 PWV, the adjusted MAE of GLPW, GFPW, and GMPW models are reduced, and the GMPW model performs better.

As shown in Figure 5, the adjusted Bias values of the GLPW, GFPW, and GMPW models decrease significantly in each season, indicating that the systematic differences between ERA5 PWV and GNSS PWV have been effectively eliminated. Therefore, the unadjusted ERA5 PWV exhibits significant negative Biases in spring, summer, and fall in the TP and SC subregions. The Biases of the adjusted GFPW and GMPW models generally show positive Biases in the four subregions and four seasons. The Bias of the GMPW model is lower than that of the GFPW model, indicating that the stability of the GMPW model is better. This also shows that the accuracy of ERA5 PWV before adjustment varies in different subregions in each season and is unevenly distributed.

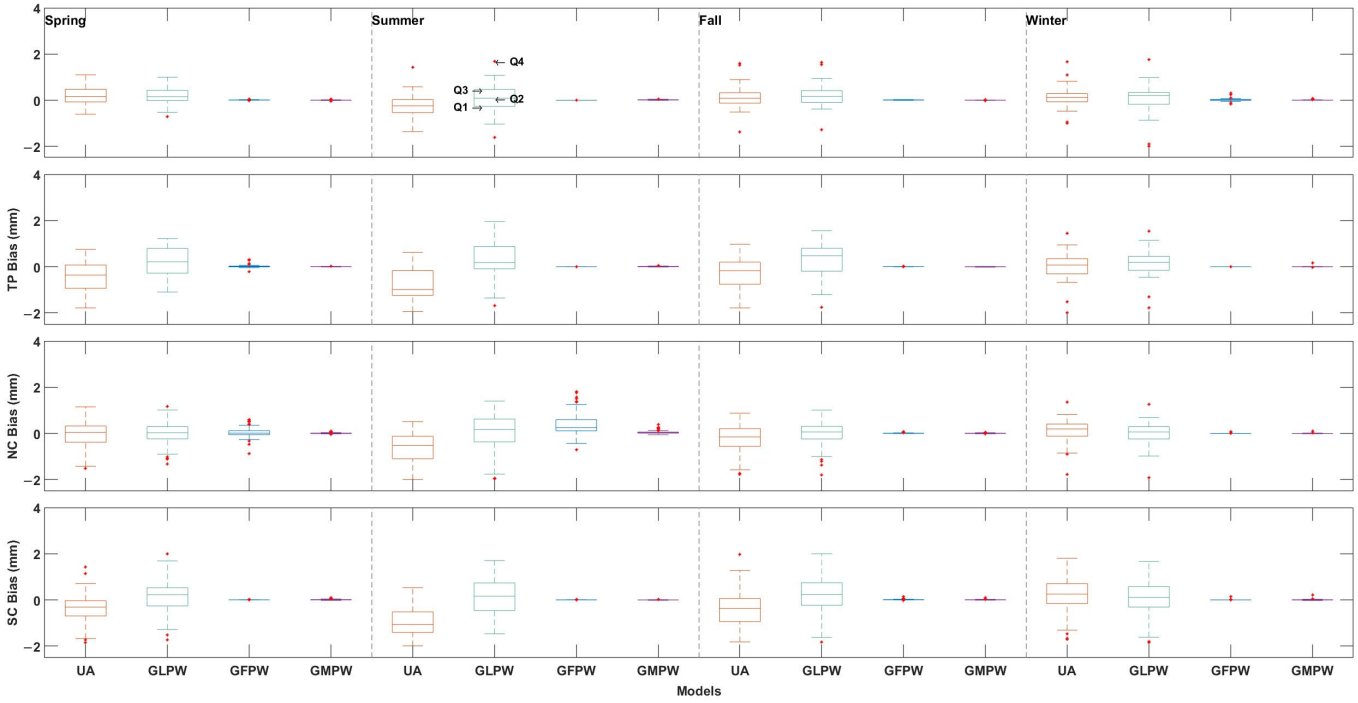


**Figure 5.** The mean Bias between different models in different seasons and subregions from 2016 to 2018 (Q1 and Q3 of the box represent the first and third quartiles, respectively; the distance of Q1 and Q3 reflects the degree of fluctuation of data; Q2 is the median value, which reflects the average level of data; Q4 represents the outlier).

As shown in Figure 6, the RMSE of unadjusted ERA5 PWV in the NWC subregion compared with GNSS PWV and the RMSE after adjustment by the GLPW model across four seasons is 1.43/0.83 mm (spring), 2.09/1.07 mm (summer), 1.40/0.84 mm (fall) and 0.92/0.53 mm (winter), respectively. Compared to the unadjusted RMSE, the RMSE of GFPW and GMPW models in the corresponding seasons decreased by 0.72/0.86 mm (50.34%/60.13%), 1.11/1.26 mm (53.11%/60.28%), 0.75/0.76 mm (53.57%/54.28%) and 0.44/0.46 mm (47.82%/50.00%), respectively. The optimization performance of the GMPW model is commensurate in four seasons, and the accuracy optimization of the GFPW model is more pronounced in summer and winter. The RMSE improvement of the GMPW model in the four seasons is superior to that of the GFPW model by 0.14 mm (9.79%), 0.15 mm

(7.17%), 0.01 mm (0.71%) and 0.02 mm (2.17%), correspondingly. This indicates that the accuracy of the GMPW model is better in spring and summer, and the accuracy of the two models is equivalent in fall and winter.

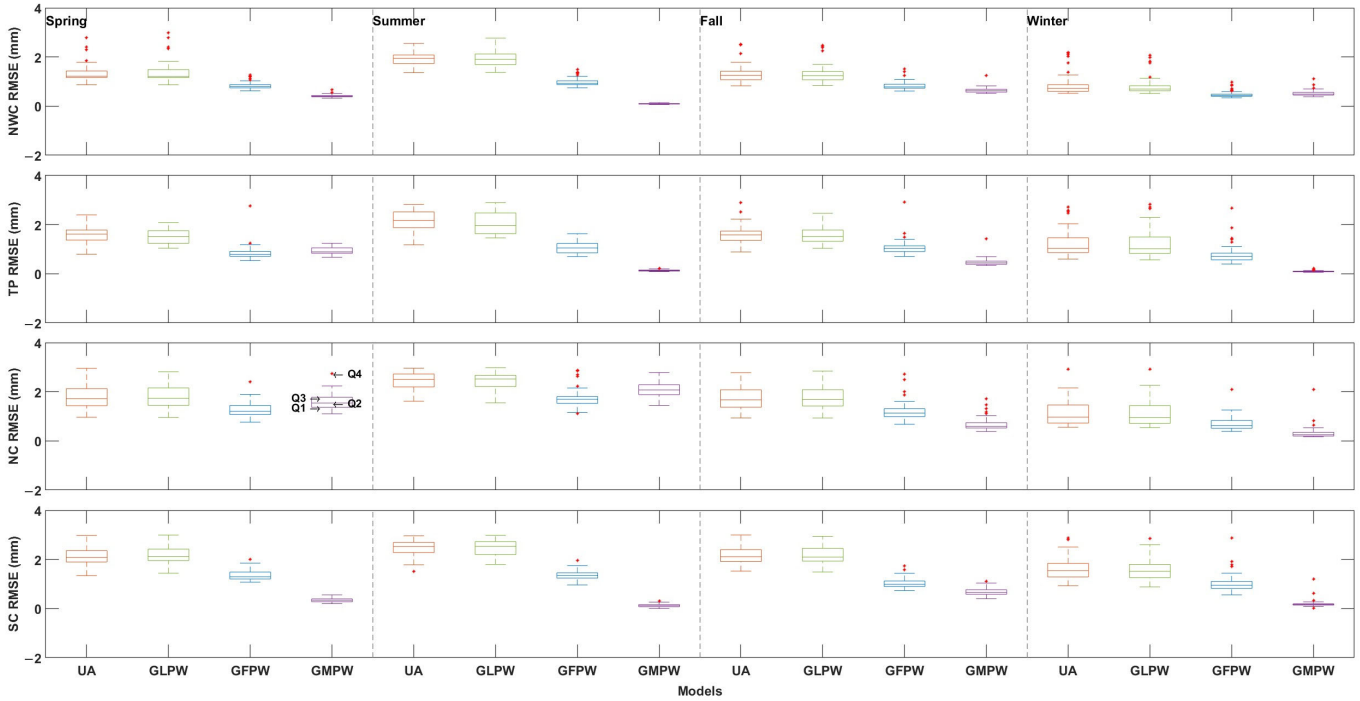


**Figure 6.** The mean RMSE between different models in different seasons and subregions from 2016 to 2018 (Q1 and Q3 of the box represent the first and third quartiles, respectively; the distance of Q1 and Q3 reflects the degree of fluctuation of data; Q2 is the median value, which reflects the average level of data; Q4 represents the outlier).

Compared with the GNSS PWV of the TP subregion, the unadjusted RMSE and the RMSE after adjustment by the GLPW model for the four seasons are 1.73/1.04 mm, 2.42/1.34 mm, 1.82/1.16 mm, and 1.33/1.08 mm, respectively. The RMSE adjusted by GFPW and GMPW models reduced by 0.8/0.87 mm (46.24%/50.28%), 1.50/1.58 mm (61.98%/65.28%), 0.67/0.94 mm (36.81%/51.64%) and 0.53/0.82 mm (39.84%/61.65%) compared to the unadjusted RMSE, respectively in the four seasons. This implies that GFPW and GMPW models show significant optimization performance in spring and summer. The RMSE improvement values between the GMPW and GFPW models for each season differ by 0.07 mm (4.04%), 0.08 mm (3.30%), 0.27 mm (14.83%) and 0.29 mm (21.80%), respectively. Therefore, the accuracy of the GMPW model in the TP subregion is equivalent in four seasons.

Compared with the GNSS PWV of the NC subregion, the unadjusted RMSE and the RMSE after adjustment by the GLPW model for the four seasons are 1.85/1.62 mm, 2.73/2.15 mm, 1.81/1.77 mm, and 1.17/1.13 mm, respectively. The RMSE adjusted by GFPW and GMPW models reduced by 0.56/0.68 mm (30.27%/36.75%), 0.85/0.99 mm (31.13%/36.26%), 0.45/0.99 mm (24.86%/54.69%) and 0.64/0.69 mm (54.70%/58.97%), respectively in each season. This implies that GFPW and GMPW models show significant optimization performance in four seasons, with improvements of 24–54% and 36–58%, respectively. The RMSE improvement values between the GFPW and GMPW models for each season differ by 0.12 mm (6.48%), 0.14 mm (5.12%), 0.54 mm (29.83%) and 0.05 mm (4.27%), respectively. This indicates that the accuracy of the GMPW model in the NC subregion is better in fall, while it is equivalent in spring, summer, and winter.

Compared with the GNSS PWV of the SC subregion, the unadjusted RMSE and the RMSE after adjustment by the GLPW model for the four seasons are 2.36/2.14 mm,

2.86/2.70 mm, 2.59/2.03 mm, and 1.99/1.91 mm, respectively. The RMSE adjusted by GFPW and GMPW models reduced by 1.02/1.44 mm (43,22%/58.47%), 1.44/1.83 mm (50.34%/63.98%), 1.11/1.52 mm (42.85%/58.65%) and 0.80/1.23 mm (40.20%/61.80%) compared to the unadjusted RMSE, respectively. This implies that GFPW and GMPW models show significant optimization performance in summer and fall. The RMSE improvement values between the GFPW and GMPW models for each season differ by 0.36 mm (15.25%), 0.39 mm (13.63%), 0.41 mm (15.83%), and 0.43 mm (21.60%). Therefore, the accuracy of the GMPW model in the SC subregion is equivalent in four seasons.

The results indicate that the accuracy of ERA5 PWV has been significantly improved after model adjustment, with the systematic differences between ERA5 PWV and GNSS PWV almost disappearing. Moreover, the GMPW model outperforms the GFPW model overall, demonstrating a significant improvement in RMSE accuracy during the summer and a slight enhancement in the fall and winter. The larger PWV errors in summer might result from higher water vapor content, while the reduced errors in fall and winter could stem from less variability in meteorological parameters and water vapor. Thus, PWV adjustment models that account for seasonal differences exhibit better performance and contribute to the production of high-quality PWV products in China.

### *4.2. Spatiotemporal Properties Analysis*

To evaluate the temporal and spatial characteristics of the optimization performance of the PWV adjustment model, we applied seasonal PWV subregion adjustment models to adjust the corresponding ERA5 PWV. Figures 7 and 8 show the distributions of Bias and RMSE between ERA5 PWV and GNSS PWV before and after optimization. The Bias and RMSE between unadjusted ERA5 PWV and GNSS PWV are notably high, especially in the southeastern coastal subregions. The adjusted Bias is nearly zero, and the overall RMSE has significantly decreased, suggesting that the PWV adjustment model effectively reduces systematic errors.

As shown in Figure 7, the unadjusted ERA5 PWV in the NC subregion shows a pronounced positive Bias in spring and winter while exhibiting a significant negative Bias in the other subregions. This indicates that the accuracy of unadjusted ERA5 PWV at different subregional sites varies and exhibits notable regional distribution characteristics. Moreover, the Bias in the adjusted ERA5 PWV has significantly decreased across all seasons, indicating that the spatial variability and land–sea variability of PWV have improved from high latitudes to low latitudes and from coastal to inland areas. Therefore, it can be concluded that the GFPW and GMPW models can effectively adjust the Bias between ERA5 PWV and GNSS PWV.

As shown in Figure 8, the RMSE after adjustment by the GLPW model is basically consistent with that before adjustment. This shows that the linear model is not very suitable for ERA5PWV adjustment in China. After adjustment by GFPW and GMPW, the seasonal RMSE of ERA5 PWV in each subregion is significantly reduced to a range of 0–2 mm, with an especially notable improvement in the SC subregion. It can be seen from Figure 7 that the adjustment effect of the GMPW model on the NC subregion in summer is lower than the adjustment accuracy of the GFPW model. This may be because the summer climate changes are complex, and the GMPW model does not apply the ERA5 PWV adjustment for this site. The variations in PWV across different subregions are associated with geographical conditions, typically exhibiting a significant decrease from the southeastern coastal areas to the northwestern inland subregions, with the highest values observed in the southeastern coastal areas.

Furthermore, the GMPW model effectively adjusted the PWV differences between coastal and inland areas in the SC subregion, resulting in a more consistent RMSE distribution of ERA5 PWV across these areas compared to the unadjusted ERA5 PWV. The RMSE of ERA5 PWV adjusted by the GFPW model in the southwestern coastal subregion shows a significant difference compared to the inland areas, especially in three seasons other than winter.

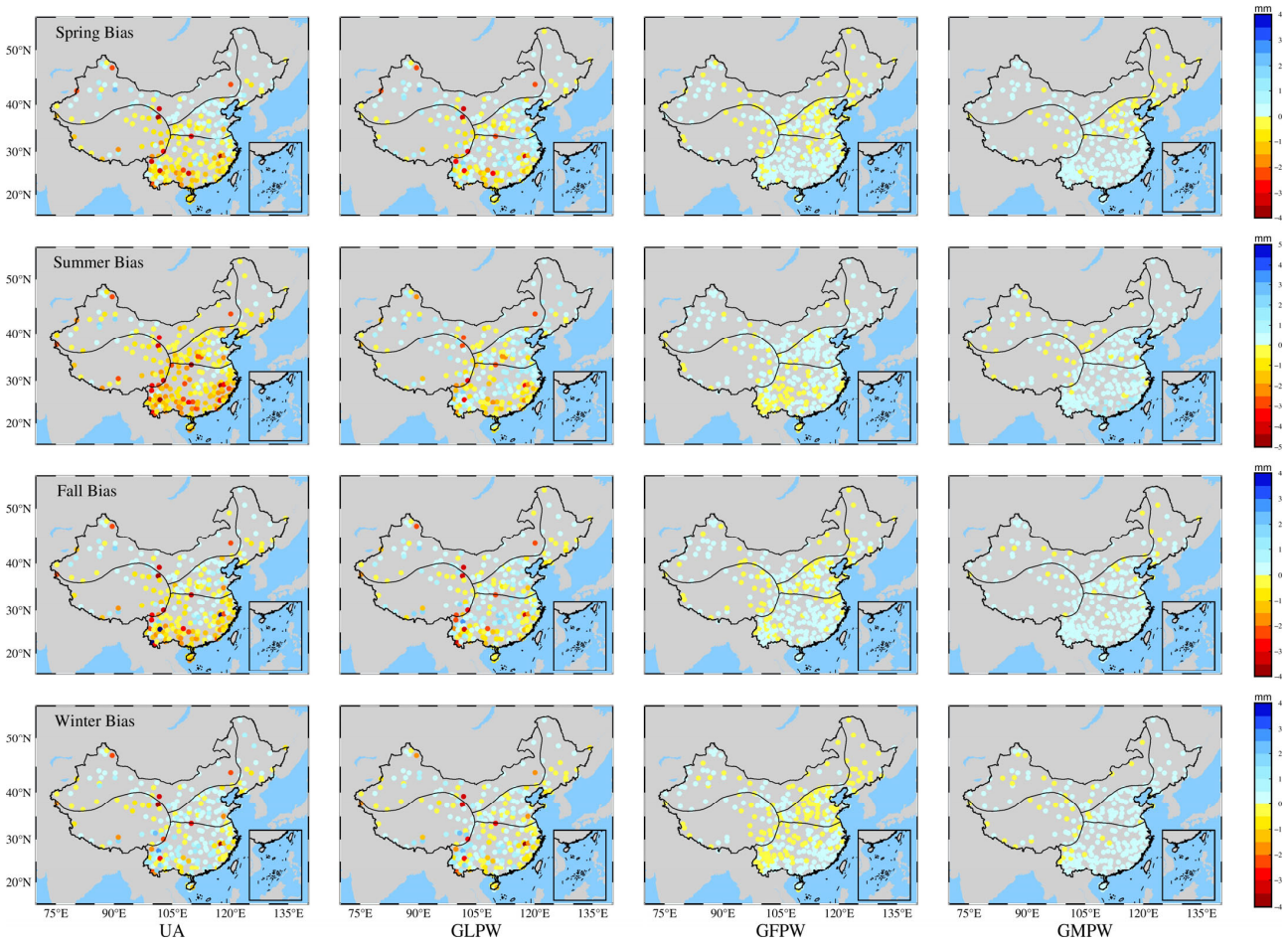


**Figure 7.** Site distribution map of Bias between ERA5 PWV and GNSS PWV before and after adjustment (UA is the unadjusted result, GLPW, GFPW, and GMPW are different adjustment models).

The Bias and RMSE of unadjusted ERA5 PWV across the entire area range from −1.42 to 0.31 mm and 0.92 to 2.86 mm, respectively. After adjustment by the GLPW model, the RMSE distribution of ERA5 PWV in each subregion is generally consistent, ranging from 0.83 to 2.15 mm. For the GFPW model, the RMSE of adjusted ERA5 PWV in the NC, TP, and NWC subregions is concentrated within the range of 0.41 mm to 1.74 mm. After adjustment by the GMPW model, the RMSE distribution of ERA5 PWV in each subregion is generally consistent, ranging from 0.14 to 1.17 mm. In the SC subregion, following adjustment by the GFPW model, the RMSE values differ significantly between the southwest coastal area and the inland sites, with differences ranging from 1 to 2 mm. Compared to the unadjusted ERA5 PWV in the SC subregion, the RMSE differences for GFPW and GMPW models in spring, summer, fall, and winter are 1.34/0.78, 1.42/0.83, 1.48/0.85, and 1.19/0.06 mm, respectively. This may be related to the obvious climate change in the SC subregion and the more obvious water vapor fluctuations in the three seasons except winter [71].

In conclusion, the GLPW model has the worst accuracy in adjusting ERA5 PWV. Both the GFPW and GMPW adjustment models effectively address the accuracy differences between ERA5 PWV and GNSS PWV, demonstrating robust accuracy and applicability. The GMPW model notably enhances the accuracy disparities between land and sea in ERA5 PWV and exhibits superior applicability in the SC subregion.

To evaluate the PWV adjustment model more comprehensively, we randomly selected 70 sites that did not participate in the modeling and applied seasonal PWV subregion adjustment models to adjust the corresponding ERA5 PWV. Taking the GNSS PWV as the reference, the Bias, MAE, and RMSE between the adjusted ERA5 PWV and the unadjusted ERA5 PWV of the GLPW, GFPW, and GMPW models are summarized in Table 7.

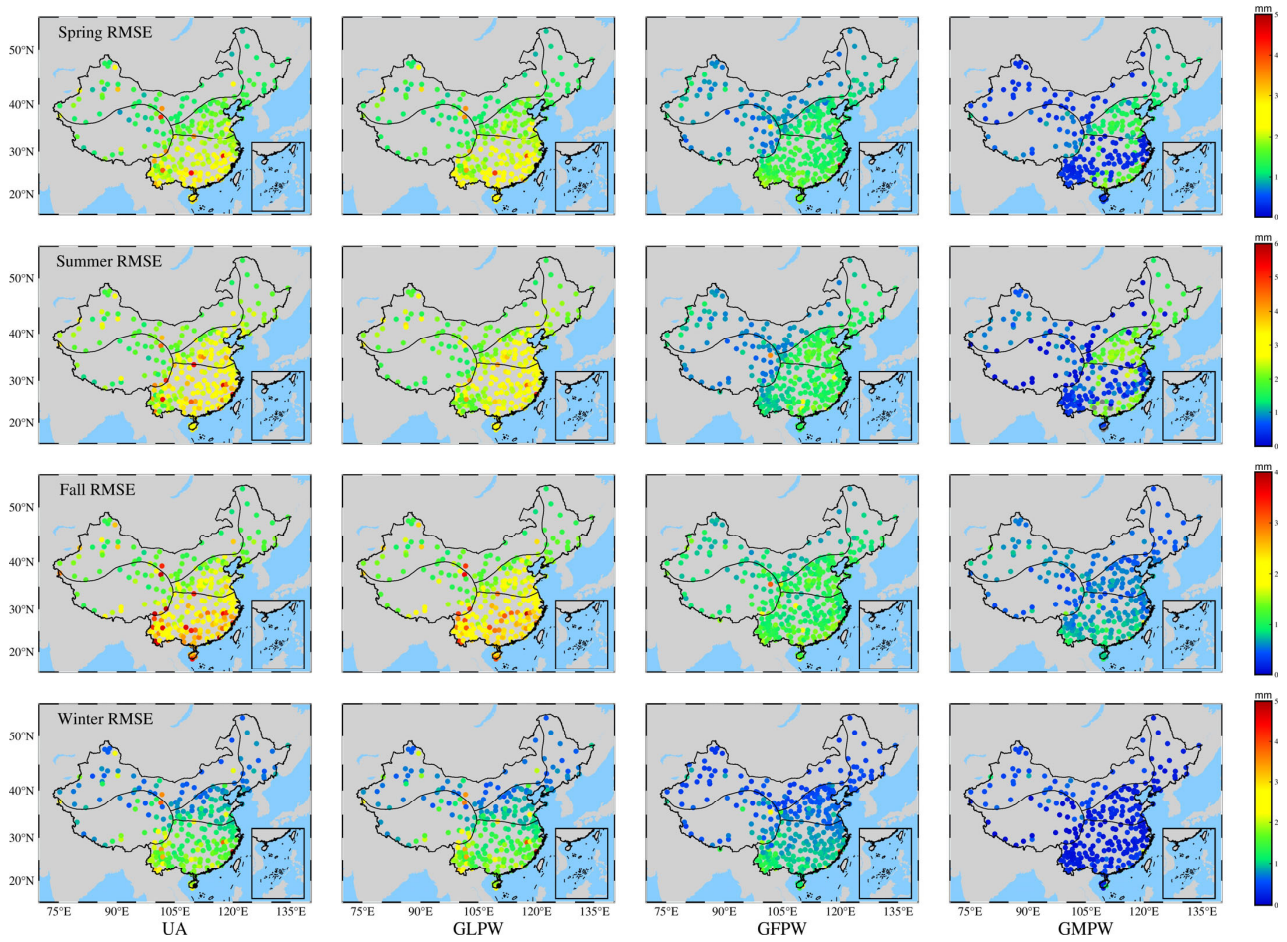


**Figure 8.** Site distribution map of RMSE between ERA5 PWV and GNSS PWV before and after adjustment (UA is the unadjusted result, GLPW, GFPW, and GMPW are different adjustment models).

**Table 7.** The external accuracy statistics between the unadjusted ERA5 PWV and ERA5 PWV adjusted by GLPW, GFPW, and GMPW models using GNSS PWV as the reference (The unit is mm, and the UA represents "Unadjusted").

| Subregion | | Bias | | | | MAE | | | | RMSE | | | |
|---|---|---|---|---|---|---|---|---|---|---|---|---|---|
| | | UA | GLPW | GFPW | GMPW | UA | GLPW | GFPW | GMPW | UA | GLPW | GFPW | GMPW |
| NWC | Spring | −0.76 | −0.22 | 0.05 | −0.01 | 1.61 | 1.16 | 1.15 | 1.05 | 2.05 | 1.48 | 1.47 | 1.37 |
| | Summer | −1.92 | −0.89 | −0.51 | −0.2 | 2.91 | 2.54 | 1.82 | 1.75 | 4.67 | 3.19 | 2.23 | 2.16 |
| | Fall | −0.47 | −0.30 | −0.09 | −0.05 | 1.22 | 1.02 | 1.14 | 1.13 | 1.62 | 1.48 | 1.47 | 1.36 |
| | Winter | 0.08 | −0.32 | 0.07 | 0.05 | 1.08 | 0.71 | 0.68 | 0.65 | 1.32 | 0.89 | 0.85 | 0.83 |
| TP | Spring | −1.46 | −0.35 | −0.27 | 0.05 | 1.90 | 1.62 | 1.58 | 1.31 | 2.35 | 2.04 | 2.02 | 1.07 |
| | Summer | −0.88 | −0.46 | −0.35 | 0.35 | 2.79 | 2.27 | 2.23 | 1.89 | 3.19 | 2.80 | 2.75 | 2.40 |
| | Fall | 0.97 | 0.51 | −0.41 | 0.03 | 3.18 | 2.39 | 1.74 | 1.65 | 4.14 | 3.15 | 2.21 | 2.14 |
| | Winter | −0.77 | −0.49 | 0.36 | 0.01 | 1.67 | 1.29 | 1.24 | 0.96 | 2.11 | 1.61 | 1.58 | 1.27 |
| NC | Spring | −3.84 | −3.17 | 0.17 | 0.16 | 4.90 | 3.36 | 1.27 | 1.27 | 4.68 | 4.13 | 1.76 | 1.66 |
| | Summer | 0.38 | −0.31 | −0.29 | −0.02 | 2.41 | 2.20 | 2.05 | 2.00 | 3.03 | 2.79 | 2.55 | 2.52 |
| | Fall | −0.42 | −0.39 | 0.16 | 0.01 | 1.59 | 1.35 | 1.22 | 1.21 | 2.14 | 1.82 | 1.62 | 1.60 |
| | Winter | −1.08 | −0.83 | 0.21 | 0.09 | 1.38 | 1.02 | 0.76 | 0.74 | 1.80 | 1.35 | 0.97 | 0.95 |
| SC | Spring | −1.23 | −0.61 | −0.73 | 0.06 | 2.68 | 1.76 | 1.94 | 1.89 | 3.37 | 2.23 | 2.45 | 2.39 |
| | Summer | −2.65 | −2.49 | −1.52 | −0.34 | 3.92 | 3.66 | 2.60 | 2.28 | 4.72 | 4.29 | 3.16 | 2.83 |
| | Fall | −2.98 | −2.89 | −0.81 | −0.29 | 3.94 | 3.95 | 2.00 | 1.89 | 4.78 | 4.63 | 2.51 | 2.39 |
| | Winter | −1.75 | −1.53 | 0.48 | 0.38 | 3.27 | 3.05 | 1.47 | 1.43 | 3.52 | 3.48 | 1.81 | 1.79 |
| China | Spring | −1.82 | −1.08 | −0.19 | 0.06 | 2.77 | 1.97 | 1.48 | 1.38 | 3.11 | 2.47 | 1.92 | 1.62 |
| | Summer | −1.26 | −1.03 | −0.66 | −0.05 | 3.00 | 2.66 | 2.17 | 1.98 | 3.90 | 3.26 | 2.67 | 2.47 |
| | Fall | −0.72 | −0.76 | −0.28 | −0.07 | 2.48 | 2.17 | 1.52 | 1.47 | 3.92 | 3.27 | 1.95 | 1.87 |
| | Winter | −0.88 | −0.79 | 0.28 | 0.13 | 1.85 | 1.51 | 1.03 | 0.94 | 2.18 | 1.83 | 1.30 | 1.21 |

As shown in Table 7, the Bias adjusted by the models GFPW and GMPW are basically close to 0 mm, which shows that the systematic differences between ERA5 PWV and GNSS PWV are basically eliminated. The Bias adjusted by model GLPW is slightly lower than before unadjusted, but there is still a certain Bias, which shows that the GLPW model is less effective in adjusting ERA5 PWV. For MAE, the ranges of the GLPW model in the NWC, TP, NC, and SC subregions are 0.71–2.54 mm, 1.29–2.39 mm, 1.02–3.36 mm, and 1.76–3.95 mm, respectively. For MAE, the ranges of the GFPW model in the NWC, TP, NC, and SC subregions are 0.68–1.82 mm, 1.24–2.23 mm, 0.76–2.05 mm, and 1.47–2.60 mm, respectively, while the value range of the GMPW model is 0.65–1.75 mm, 0.96–1.89 mm, 0.74–2.00 mm, 1.43–2.28 mm. Compared with unadjusted PWV, the adjusted MAE of GLPW, GFPW, and GMPW models are reduced, and the GMPW model performs better.

As shown in Figures 9 and 10, the Bias and RMSE spatial distribution between ERA5 PWV and GNSS PWV before and after adjustment. In Figure 8, the Bias after adjustment of the GLPW model is basically the same as before the adjustment, which shows that the adjustment accuracy of the linear model is poor and is not suitable for ERA5 PWV water vapor adjustment. In addition, the Bias of the ERA5 PWV corrected by the GFPW and GMPW models is significantly reduced in each subregion, and the GMPW model adjustment results are better. After adjustment by GFPW and GMPW, the seasonal Bias of each partition of ERA5 PWV was significantly reduced to approximately 0, with the NC subregion improving particularly significantly. This shows that both the GFPW and GMPW models can adjust the ERA5 PWV of external sites well.

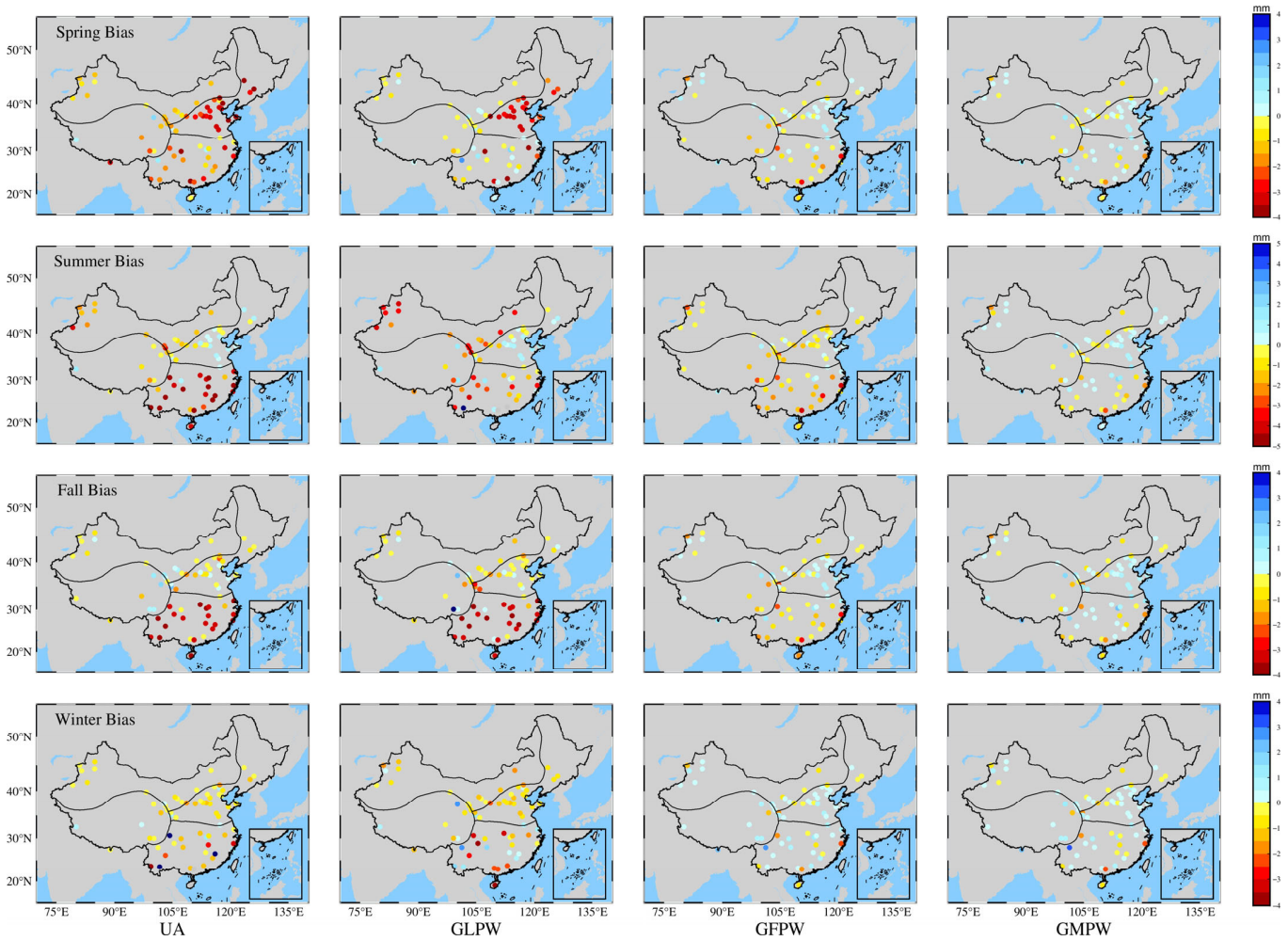


**Figure 9.** External sites distribution map of Bias between ERA5 PWV and GNSS PWV before and after adjustment (UA is the unadjusted result, GLPW, GFPW, and GMPW are different adjustment models).

As shown in Figure 10, the RMSE of ERA5 PWV at the external site of the GLPW model is basically the same after adjustment as before adjustment, which indicates that the linear model is not suitable for PWV adjustment in China. After adjustment by the GFPW and GMPW models, the seasonal RMSE in each subregion of the ERA5 PWV was significantly reduced to the range of 1–2 mm, with the NC subregion improving particularly significantly in fall and winter. In spring and summer, the adjusted RMSE of the GLPW model is around 2.5 mm, and the adjusted RMSE of the GFPW and GMPW models is around 2.0 mm. In addition, in the summer of the GFPW model, the RMSE value of the QHTR site on the west side of the TP subregion is very large, about 5 mm. This may be because the site is surrounded by high mountains near its location, resulting in complex precipitation there [72]. Therefore, the adjusted RMSE of ERA5 PWV is larger. In conclusion, the GFPW and GMPW models are more suitable for China ERA5 PWV adjustment and have higher accuracy than the GLPW model.

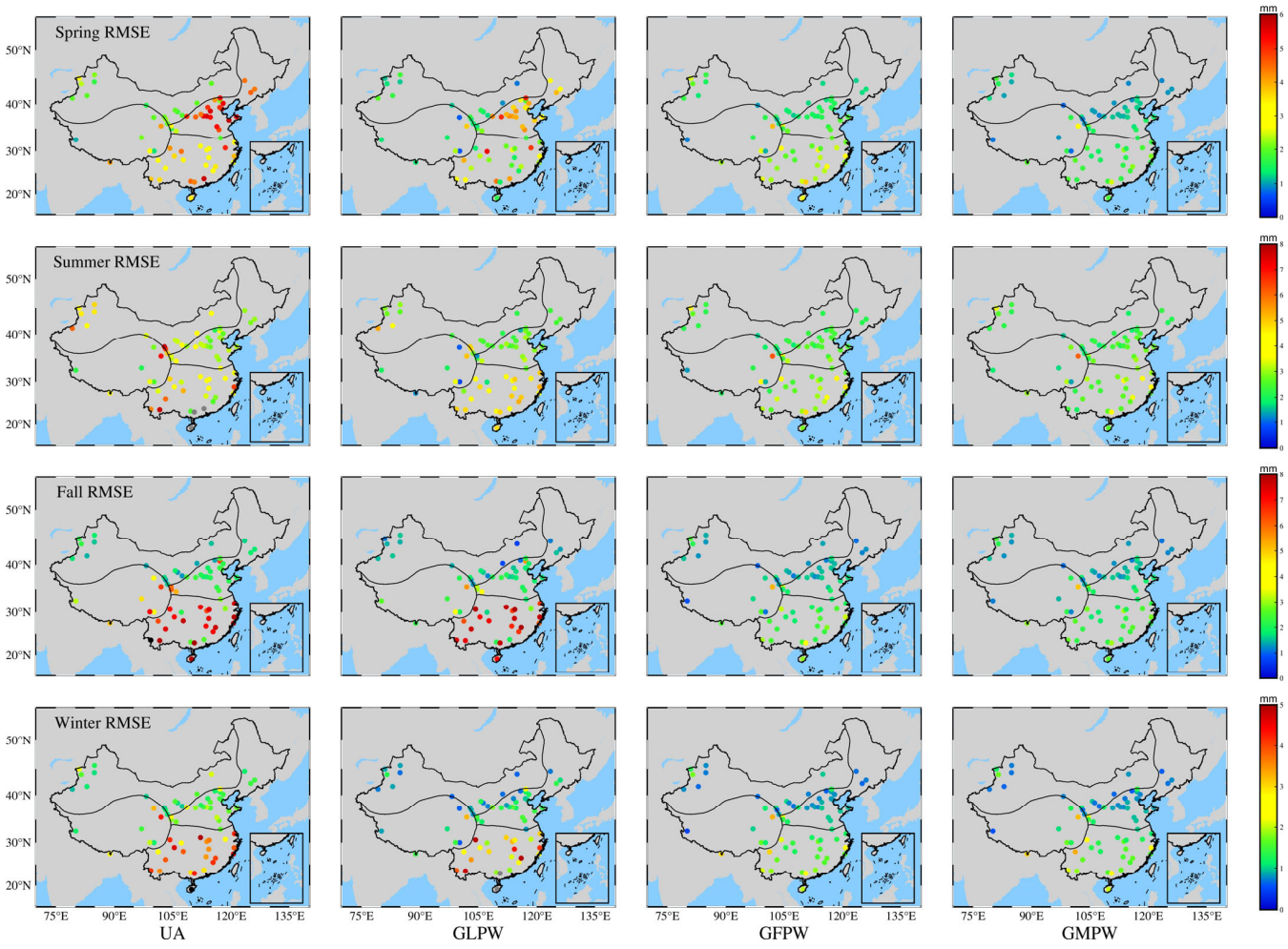


**Figure 10.** External sites distribution map of RMSE between ERA5 PWV and GNSS PWV before and after adjustment (UA is the unadjusted result, GLPW, GFPW, and GMPW are different adjustment models).

## 5. Conclusions

Machine learning algorithms proficiently discern the intricate nonlinear associations inherent in various PWV datasets, facilitating the enhancement of PWV datasets and the production of PWV products characterized by high precision and resolution. Current PWV adjustment models inadequately address the comprehensive assessment of error distribution patterns among diverse PWV datasets and the spatiotemporal applicability

of adjustment models. Therefore, this study constructs PWV adjustment models based on meteorological parameters (GMPW model) and non-meteorological parameters (GFPW model) by introducing the GRNN algorithm. A linear model GLPW was established to compare model accuracy. Through model comparison and accuracy verification, the RMSE of seasonal ERA5 PWV in each subregion was significantly reduced, and the accuracy before and after the overall adjustment was about 0–4 mm and 0–2 mm. Adjusted overall ERA5 PWV Bias in four subregions of GLPW, GFPW, and GMPW models floats at 0 mm.

The RMSE of the four seasons relative to the unadjusted ERA5 PWV in the GLPW, GFPW, and GMPW models are 24%/42%/51%, 28%/48%/56%, 23%/39%/55%, and 14%/45 are %/59%, respectively. The RMSE change amplitudes of the four subregions (NWC, NC, TP, and SC) after adjustment in the GLPW, GFPW, and GMPW models are 0.54/0.50/0.37 mm, 0.37/0.35/0.30 mm, 1.35/1.02/0.31 mm, and 0.79/0.31/0.29 mm, respectively. Therefore, compared to the GFPW model, the GMPW model exhibits superior performance in the NWC subregion during spring and summer, in the TP subregion during fall and winter, in the SC subregion during summer and fall, and in the NC subregion across all four seasons. In addition, compared with the linear model GLPW, the GFPW and GMPW models have better adjustment capabilities. After conducting accuracy tests using GNSS PWV data not involved in the modeling, we found that the RMSE of the GLPW, GFPW, and GMPW models relative to the unadjusted ERA5 PWV in the four seasons are 20%/38%/47%, 16%/31%/36%, 16%/50%/52 and 16%/ 40%/44%, respectively. Therefore, the GFPW and GMPW models have better ERA5 PWV adjustment performance than the GLPW model in China, with the GMPW model having the best performance.

In conclusion, considering the seasonal and geographical characteristics of water vapor in China, the PWV adjustment model based on the GRNN algorithm can effectively reduce the systematic Bias in ERA5 PWV data and exhibits good accuracy and reliability. Compared with unadjusted ERA5 PWV and ERA5 PWV adjusted by models GLPW and GFPW, the GMPW model has superior spatial stability and can significantly improve the difference between coastal and inland ERA5 PWV and GNSS PWV. GFPW and GMPW models can generate PWV products with high spatial and temporal resolution, providing a reference for GNSS-ERA5 PWV fusion research. Future endeavors will explore different ERA5-PWV adjustment models and then use high-precision adjustment models for PWV fusion and water vapor monitoring.

**Author Contributions:** H.P.: Conceptualization, Methodology, Formal analysis, Validation, Data curation, Writing—original draft, Writing—review and editing. L.Z.: Conceptualization, Methodology, Formal analysis, Software, Writing—original draft. W.L.: Conceptualization, Methodology, Formal analysis, Data curation. X.W.: Validation, Software, Data curation. Y.W.: Investigation, Writing—review and editing, Funding acquisition. L.H.: Investigation, Funding acquisition. All authors have read and agreed to the published version of the manuscript.

**Funding:** This study is supported by the Guangxi Natural Science Foundation of China, grant number 2023GXNSFAA026434, 2023GXNSFAA026355 and 2023GXNSFBA026350; the National Natural Science of China, grant number 42201463; the Special Fund of Guangxi Science and Technology Base and Talent, grant number Guike AD22035158 and Guike AD23026167; and the "Ba Gui Scholars" program of the provincial government of Guangxi.

**Data Availability Statement:** The GNSS data from the China Meteorological Administration (CMA) can be accessed from https://data.cma.cn/en/ (accessed on 1 June 2023). The radiosonde data are obtained from http://www1.ncdc.noaa.gov/pub/data/igra/ (accessed on 1 June 2023). The ERA5 data are available at https://cds.climate.copernicus.eu/cdsapp#!/search?type=dataset (accessed on 1 June 2023). All the figures in this manuscript are generated by MATLAB 2023 and GMT 6.4 software.

**Acknowledgments:** The authors thank CMONOC (Crustal Movement Observation Network of China) for providing GPS data, ECMWF (European Centre for Medium-Range Weather Forecasts) for providing the ERA5 grid data, and IGRA (Integrated Global Radiosonde Archive) for radiosonde data in this study.

**Conflicts of Interest:** The authors declare no conflicts of interest.

## References


1. Gong, Y.Z.; Liu, Z.Z.; Chan, P.W.; Hon, K.K. Assimilating GNSS PWV and radiosonde meteorological profiles to improve the PWV and rainfall forecasting performance from the Weather Research and Forecasting (WRF) model over the South China. *Atmos. Res.* **2023**, *286*, 106677. [CrossRef]
2. Li, H.B.; Wang, X.M.; Choy, S.; Jiang, C.H.; Wu, S.Q.; Zhang, J.L.; Qiu, C.; Zhou, K.; Li, L.; Fu, E.R.; et al. Detecting heavy rainfall using anomaly-based percentile thresholds of predictors derived from GNSS-PWV. *Atmos. Res.* **2022**, *265*, 105912. [CrossRef]
3. Wu, F.; Li, D.; Zhao, J.; Jiang, H.; Luo, X. SDIPPWV: A novel hybrid prediction model based on stepwise decomposition-integration-prediction avoids future information leakage to predict precipitable water vapor from GNSS observations. *Sci. Total Environ.* **2024**, *933*, 173116. [CrossRef] [PubMed]
4. Zhao, T.B.; Dai, A.G.; Wang, J.H. Trends in Tropospheric Humidity from 1970 to 2008 over China from a Homogenized Radiosonde Dataset. *J. Clim.* **2012**, *25*, 4549–4567. [CrossRef]
5. Xiong, Z.H.; Zhang, B.; Sang, J.Z.; Sun, X.G.; Wei, X.M. Fusing Precipitable Water Vapor Data in CHINA at Different Timescales Using an Artificial Neural Network. *Remote Sens.* **2021**, *13*, 1720. [CrossRef]
6. Yunck, T.P.; Liu, C.H.; Ware, R. A history of GPS sounding. *Terr. Atmos. Ocean. Sci.* **2000**, *11*, 1–20. [CrossRef]
7. Trenberth, K.E.; Fasullo, J.; Smith, L. Trends and variability in column-integrated atmospheric water vapor. *Clim. Dyn.* **2005**, *24*, 741–758. [CrossRef]
8. Ning, T.; Elgered, G.; Willén, U.; Johansson, J.M. Evaluation of the atmospheric water vapor content in a regional climate model using ground-based GPS measurements. *J. Geophys. Res. Atmos.* **2013**, *118*, 329–339. [CrossRef]
9. Elliott, W.P.; Gaffen, D.J. On the Utility of Radiosonde Humidity Archives for Climate Studies. *Bull. Am. Meteorol. Soc.* **1991**, *72*, 1507–1520. [CrossRef]
10. Lindstrot, R.; Preusker, R.; Diedrich, H.; Doppler, L.; Bennartz, R.; Fischer, J. 1D-Var retrieval of daytime total columnar water vapour from MERIS measurements. *Atmos. Meas. Technol.* **2012**, *5*, 631–646. [CrossRef]
11. Alexandrov, M.D.; Schmid, B.; Turner, D.D.; Cairns, B.; Oinas, V.; Lacis, A.A.; Gutman, S.I.; Westwater, E.R.; Smirnov, A.; Eilers, J. Columnar water vapor retrievals from multifilter rotating shadowband radiometer data. *J. Geophys. Res. Atmos.* **2009**, *114*. [CrossRef]
12. Huang, L.K.; Liu, W.; Mo, Z.X.; Zhang, H.X.; Li, J.Y.; Chen, F.D.; Liu, L.L.; Jiang, W.P. A new model for vertical adjustment of precipitable water vapor with consideration of the time-varying lapse rate. *Gps Solut.* **2023**, *27*, 170. [CrossRef]
13. Wu, M.L.; Jin, S.G.; Li, Z.C.; Cao, Y.C.; Ping, F.; Tang, X. High-Precision GNSS PWV and Its Variation Characteristics in China Based on Individual Station Meteorological Data. *Remote Sens.* **2021**, *13*, 1296. [CrossRef]
14. Hanssen, R.F.; Weckwerth, T.M.; Zebker, H.A.; Klees, R. High-resolution water vapor mapping from interferometric radar measurements. *Science* **1999**, *283*, 1297–1299. [CrossRef] [PubMed]
15. Bevis, M.; Businger, S.; Herring, T.A.; Rocken, C.; Anthes, R.A.; Ware, R.H. GPS Meteorology—Remote-Sensing of Atmospheric Water-Vapor Using the Global Positioning System. *J. Geophys. Res. Atmos.* **1992**, *97*, 15787–15801. [CrossRef]
16. Emardson, T.R.; Elgered, G.; Johansson, J.M. Three months of continuous monitoring of atmospheric water vapor with a network of Global Positioning System receivers. *J. Geophys. Res. Atmos.* **1998**, *103*, 1807–1820. [CrossRef]
17. Niell, A.E.; Coster, A.J.; Solheim, F.S.; Mendes, V.B.; Toor, P.C.; Langley, R.B.; Upham, C.A. Comparison of measurements of atmospheric wet delay by radiosonde, water vapor radiometer, GPS, and VLBI. *J. Atmos. Ocean. Technol.* **2001**, *18*, 830–850. [CrossRef]
18. Huang, L.K.; Mo, Z.X.; Xie, S.F.; Liu, L.L.; Chen, J.; Kang, C.L.; Wang, S.T. Spatiotemporal characteristics of GNSS-derived precipitable water vapor during heavy rainfall events in Guilin, China. *Satell. Navig.* **2021**, *2*, 13. [CrossRef]
19. Westwater, E.R. Remote sensing of tropospheric temperature and water vapor by integrated observing systems—The remote sensing lecture. *Bull. Am. Meteorol. Soc.* **1997**, *78*, 1991–2006. [CrossRef]
20. Zhang, Q.; Ye, J.H.; Zhang, S.C.; Han, F. Precipitable Water Vapor Retrieval and Analysis by Multiple Data Sources: Ground-Based GNSS, Radio Occultation, Radiosonde, Microwave Satellite, and NWP Reanalysis Data. *J. Sens.* **2018**, *2018*, 3428303. [CrossRef]
21. Zhang, B.; Yao, Y.B.; Xin, L.Y.; Xu, X.Y. Precipitable water vapor fusion: An approach based on spherical cap harmonic analysis and Helmert variance component estimation. *J. Geod.* **2019**, *93*, 2605–2620. [CrossRef]
22. Liu, W.; Zhang, L.L.; Xiong, S.; Huang, L.K.; Xie, S.F.; Liu, L.L. Investigating the ERA5-Based PWV Products and Identifying the Monsoon Active and Break Spells with Dense GNSS Sites in Guangxi, China. *Remote Sens.* **2023**, *15*, 4710. [CrossRef]
23. Khaniani, A.S.; Nikraftar, Z.; Zakeri, S. Evaluation of MODIS Near-IR water vapor product over Iran using ground-based GPS measurements. *Atmos. Res.* **2020**, *231*, 104657. [CrossRef]
24. Bai, J.N.; Lou, Y.D.; Zhang, W.X.; Zhou, Y.Z.; Zhang, Z.Y.; Shi, C. Assessment and calibration of MODIS precipitable water vapor products based on GPS network over China. *Atmos. Res.* **2021**, *254*, 105504. [CrossRef]
25. Zhu, D.T.; Zhang, K.F.; Yang, L.; Wu, S.Q.; Li, L.J. Evaluation and Calibration of MODIS Near-Infrared Precipitable Water Vapor over China Using GNSS Observations and ERA-5 Reanalysis Dataset. *Remote Sens.* **2021**, *13*, 2761. [CrossRef]
26. Wang, X.Z.; Chen, F.Y.; Ke, F.Y.; Xu, C. An Empirical Grid Model for Precipitable Water Vapor. *Remote Sens.* **2022**, *14*, 6174. [CrossRef]
27. Alshawaf, F.; Fersch, B.; Hinz, S.; Kunstmann, H.; Mayer, M.; Meyer, F.J. Water vapor mapping by fusing InSAR and GNSS remote sensing data and atmospheric simulations. *Hydrol. Earth Syst. Sci.* **2015**, *19*, 4747–4764. [CrossRef]

28. Shikhovtsev, A.Y.; Kovadlo, P.G.; Khaikin, V.B.; Kiselev, A.V. Precipitable Water Vapor and Fractional Clear Sky Statistics within the Big Telescope Alt-Azimuthal Region. *Remote Sens.* **2022**, *14*, 6221. [CrossRef]
29. Liu, J.; Li, T.R.; Xie, P.; Du, S.D.; Teng, F.; Yang, X. Urban big data fusion based on deep learning: An overview. *Inf. Fusion* **2020**, *53*, 123–133. [CrossRef]
30. Chen, F.C.; Jahanshahi, M.R. NB-CNN: Deep Learning-Based Crack Detection Using Convolutional Neural Network and Naive Bayes Data Fusion. *IEEE Trans. Ind. Electron.* **2018**, *65*, 4392–4400. [CrossRef]
31. Wang, L.L.; Xin, J.Y.; Wang, Y.S.; Li, Z.Q.; Wang, P.C.; Liu, G.R.; Wen, T.X. Validation of MODIS aerosol products by CSHNET over china. *Chin. Sci. Bull.* **2007**, *52*, 1708–1718. [CrossRef]
32. Lu, C.X.; Zhang, Y.S.; Zheng, Y.X.; Wu, Z.L.; Wang, Q.Y. Precipitable water vapor fusion of MODIS and ERA5 based on convolutional neural network. *Gps Solut.* **2023**, *27*, 15. [CrossRef]
33. Xiong, Z.H.; Sun, X.G.; Sang, J.Z.; Wei, X.M. Modify the Accuracy of MODIS PWV in China: A Performance Comparison Using Random Forest, Generalized Regression Neural Network and Back-Propagation Neural Network. *Remote Sens.* **2021**, *13*, 2215. [CrossRef]
34. Ma, X.W.; Yao, Y.B.; Zhang, B.; Du, Z. FY-3A/MERSI precipitable water vapor reconstruction and calibration using multi-source observation data based on a generalized regression neural network. *Atmos. Res.* **2022**, *265*, 105893. [CrossRef]
35. Mateus, P.; Catalao, J.; Mendes, V.B.; Nico, G. An ERA5-Based Hourly Global Pressure and Temperature (HGPT) Model. *Remote Sens.* **2020**, *12*, 1098. [CrossRef]
36. Gui, K.; Che, H.Z.; Chen, Q.L.; Zeng, Z.L.; Liu, H.Z.; Wang, Y.Q.; Zheng, Y.; Sun, T.Z.; Liao, T.T.; Wang, H.; et al. Evaluation of radiosonde, MODIS-NIR-Clear, and AERONET precipitable water vapor using IGS ground-based GPS measurements over China. *Atmos. Res.* **2017**, *197*, 461–473. [CrossRef]
37. Huang, L.K.; Jiang, W.P.; Liu, L.L.; Chen, H.; Ye, S.R. A new global grid model for the determination of atmospheric weighted mean temperature in GPS precipitable water vapor. *J. Geod.* **2019**, *93*, 159–176. [CrossRef]
38. Yuan, Q.Q.; Xu, H.Z.; Li, T.W.; Shen, H.F.; Zhang, L.P. Estimating surface soil moisture from satellite observations using a generalized regression neural network trained on sparse ground-based measurements in the continental U.S. *J. Hydrol.* **2020**, *580*, 124351. [CrossRef]
39. Li, T.W.; Shen, H.F.; Yuan, Q.Q.; Zhang, X.C.; Zhang, L.P. Estimating Ground-Level $PM_{2.5}$ by Fusing Satellite and Station Observations: A Geo-Intelligent Deep Learning Approach. *Geophys. Res. Lett.* **2017**, *44*, 11985–11993. [CrossRef]
40. Rodríguez, J.D.; Pérez, A.; Lozano, J.A. Sensitivity Analysis of *k*-Fold Cross Validation in Prediction Error Estimation. *IEEE Trans. Pattern Anal. Mach. Intell.* **2010**, *32*, 569–575. [CrossRef]
41. Altonji, J.G.; Segal, L.M.J.J.o.B.; Statistics, E. Small-sample bias in GMM estimation of covariance structures. *J. Bus. Econ. Stat.* **1996**, *14*, 353–366. [CrossRef]
42. Zhang, W.; Zhang, H.; Liang, H.; Lou, Y.; Cai, Y.; Cao, Y.; Zhou, Y.; Liu, W. On the suitability of ERA5 in hourly GPS precipitable water vapor retrieval over China. *J. Geod.* **2019**, *93*, 1897–1909. [CrossRef]
43. Hersbach, H.; Bell, B.; Berrisford, P.; Hirahara, S.; Horányi, A.; Muñoz-Sabater, J.; Nicolas, J.; Peubey, C.; Radu, R.; Schepers, D.; et al. The ERA5 global reanalysis. *Q. J. R. Meteorol. Soc.* **2020**, *146*, 1999–2049. [CrossRef]
44. Huang, L.; Zhu, G.; Liu, L.L.; Chen, H.; Jiang, W.P. A global grid model for the correction of the vertical zenith total delay based on a sliding window algorithm. *Gps Solut.* **2021**, *25*, 98. [CrossRef]
45. Huang, L.K.; Lan, S.W.; Zhu, G.; Chen, F.D.; Li, J.Y.; Liu, L.L. A global grid model for the estimation of zenith tropospheric delay considering the variations at different altitudes. *Geosci. Model Dev.* **2023**, *16*, 7223–7235. [CrossRef]
46. Huang, L.K.; Wang, X.; Xiong, S.; Li, J.Y.; Liu, L.L.; Mo, Z.X.; Fu, B.L.; He, H.C. High-precision GNSS PWV retrieval using dense GNSS sites and in-situ meteorological observations for the evaluation of MERRA-2 and ERA5 reanalysis products over China. *Atmos. Res.* **2022**, *276*, 106247. [CrossRef]
47. Muñoz-Sabater, J.; Dutra, E.; Agustí-Panareda, A.; Albergel, C.; Arduini, G.; Balsamo, G.; Boussetta, S.; Choulga, M.; Harrigan, S.; Hersbach, H.; et al. ERA5-Land: A state-of-the-art global reanalysis dataset for land applications. *Earth Syst. Sci. Data* **2021**, *13*, 4349–4383. [CrossRef]
48. Zhao, Q.Z.; Du, Z.; Yao, W.Q.; Yao, Y.B. Hybrid precipitable water vapor fusion model in China. *J. Atmos. Sol. Terr. Phys.* **2020**, *208*, 105387. [CrossRef]
49. Mo, Z.X.; Zeng, Z.L.; Huang, L.K.; Liu, L.L.; Huang, L.; Zhou, L.; Ren, C.; He, H.C. Investigation of Antarctic Precipitable Water Vapor Variability and Trend from 18 Year (2001 to 2018) Data of Four Reanalyses Based on Radiosonde and GNSS Observations. *Remote Sens.* **2021**, *13*, 3901. [CrossRef]
50. Gao, B.C.; Yang, P.; Guo, G.; Park, S.K.; Wiscombe, W.J.; Chen, B. Measurements of water vapor and high clouds over the Tibetan Plateau with the Terra MODIS instrument. *Ieee Trans. Geosci. Remote Sens.* **2003**, *41*, 895–900. [CrossRef]
51. Lindenbergh, R.; Keshin, M.; Van der Marel, H.; Hanssen, R. High resolution spatio-temporal water vapour mapping using GPS and MERIS observations. *Int. J. Remote Sens.* **2008**, *29*, 2393–2409. [CrossRef]
52. He, J.; Liu, Z.Z. Water Vapor Retrieval from MODIS NIR Channels Using Ground-Based GPS Data. *IEEE Trans. Geosci. Remote Sens.* **2020**, *58*, 3726–3737. [CrossRef]
53. Zhang, J.H.; Zuo, X.Q.; Guo, S.P.; Xie, S.F.; Yang, X.; Li, Y.N.; Yue, X.F. A New Grid Zenith Tropospheric Delay Model Considering Time-Varying Vertical Adjustment and Diurnal Variation over China. *Remote Sens.* **2024**, *16*, 2023. [CrossRef]

54. Saastamoinen, J. Atmospheric correction for the troposphere and stratosphere in radio ranging satellites. *Use Artif. Satell. Geod.* **1972**, *15*, 247–251. [CrossRef]
55. Huang, L.K.; Mo, Z.X.; Liu, L.L.; Zeng, Z.L.; Chen, J.; Xiong, S.; He, H.C. Evaluation of Hourly PWV Products Derived From ERA5 and MERRA-2 Over the Tibetan Plateau Using Ground-Based GNSS Observations by Two Enhanced Models. *Earth Space Sci.* **2021**, *8*, e2020ea001516. [CrossRef]
56. Zhang, B.; Yao, Y.B. Precipitable water vapor fusion based on a generalized regression neural network. *J. Geod.* **2021**, *95*, 36. [CrossRef]
57. Specht, D.F. A General Regression Neural Network. *IEEE Trans. Neural Netw.* **1991**, *2*, 568–576. [CrossRef] [PubMed]
58. Cigizoglu, H.K.; Alp, M. Generalized regression neural network in modelling river sediment yield. *Adv. Eng. Softw.* **2006**, *37*, 63–68. [CrossRef]
59. Kannemadugu, H.B.S.; Ranganathan, K.; Gharai, B.; Seshasai, M.V.R. GNSS-GPS derived integrated water vapor and performance assessment of ERA-5 data over India. *J. Atmos. Sol. Terr. Phys.* **2022**, *227*, 105807. [CrossRef]
60. Zhang, W.Y.; Wei, Z.W.; Wang, B.H.; Han, X.P. Measuring mixing patterns in complex networks by Spearman rank correlation coefficient. *Phys. A-Stat. Mech. Its Appl.* **2016**, *451*, 440–450. [CrossRef]
61. Gauthier, T.D. Detecting trends using Spearman's rank correlation coefficient. *Environ. Forensics* **2001**, *2*, 359–362. [CrossRef]
62. Kouba, J. Implementation and testing of the gridded Vienna Mapping Function 1 (VMF1). *J. Geod.* **2008**, *82*, 193–205. [CrossRef]
63. Ye, H.C.; Fetzer, E.J.; Wong, S.; Behrangi, A.; Olsen, E.T.; Cohen, J.; Lambrigtsen, B.H.; Chen, L.K. Impact of increased water vapor on precipitation efficiency over northern Eurasia. *Geophys. Res. Lett.* **2014**, *41*, 2941–2947. [CrossRef]
64. Kim, B.; Lee, D.W.; Park, K.Y.; Choi, S.R.; Choi, S. Prediction of plasma etching using a randomized generalized regression neural network. *Vacuum* **2004**, *76*, 37–43. [CrossRef]
65. Feng, Y.; Cui, N.B.; Gong, D.Z.; Zhang, Q.W.; Zhao, L. Evaluation of random forests and generalized regression neural networks for daily reference evapotranspiration modelling. *Agric. Water Manag.* **2017**, *193*, 163–173. [CrossRef]
66. Zhou, Q.P.; Jiang, H.Y.; Wang, J.Z.; Zhou, J.L. A hybrid model for $PM_{2.5}$ forecasting based on ensemble empirical mode decomposition and a general regression neural network. *Sci. Total Environ.* **2014**, *496*, 264–274. [CrossRef] [PubMed]
67. Fushiki, T. Estimation of prediction error by using K-fold cross-validation. *Stat. Comput.* **2011**, *21*, 137–146. [CrossRef]
68. Wong, T.T.; Yeh, P.Y. Reliable Accuracy Estimates from *k*-Fold Cross Validation. *IEEE Trans. Knowl. Data Eng.* **2020**, *32*, 1586–1594. [CrossRef]
69. Bei, L.; Yong, W.; Zesheng, L.; Wei, Z.J. The MODIS PWV correction based on CMONOC in Chinese mainland. *Acta Geod. Cartogr. Sin.* **2019**, *48*, 1207. [CrossRef]
70. Chai, T.; Draxler, R.R. Root mean square error (RMSE) or mean absolute error (MAE)?—Arguments against avoiding RMSE in the literature. *Geosci. Model Dev.* **2014**, *7*, 1247–1250. [CrossRef]
71. Lien, T.Y.; Yeh, T.K.; Hong, J.S.; Hsiao, T.Y. Variations in GPS precipitable water vapor and rainfall during the 2006–2019 Mei-yu season in Taiwan. *Adv. Space Res.* **2022**, *70*, 1375–1387. [CrossRef]
72. Shi, F.L.; Xin, J.Y.; Yang, L.K.; Cong, Z.Y.; Liu, R.X.; Ma, Y.N.; Wang, Y.S.; Lu, X.F.; Zhao, L. The first validation of the precipitable water vapor of multisensor satellites over the typical regions in China. *Remote Sens. Environ.* **2018**, *206*, 107–122. [CrossRef]